Characterizing the very-high-energy gamma-ray and broadband emission of blazar BL Lacertae

Carlos Ortega Hunter

Characterizing the very-high-energy gamma-ray and broadband emission of blazar BL Lacertae

Carlos Ortega Hunter

Memoria del **Trabajo Fin de Máster**
Máster en Física y Matemáticas (FisyMat)
Universidad de Granada
Septiembre 2024

Tutorizado por:

Dr. Jorge Otero Santos
Dr. Iván Agudo

Declaración de originalidad

D. Carlos-Axel Ortega Hunter, con DNI 46471699S, garantiza con su firma que en la realización del TFM de título "Characterizing the very-high-energy gamma-ray and broadband emission of blazar BL Lacertae" se han respetado los derechos de otros autores a ser citados cuando se han utilizado sus resultados o publicaciones.

Firmado: Carlos-Axel Ortega Hunter

Carlos Ortega

Barcelona, 6 de Septiembre de 2024

Agradecimientos

Me gustaría expresar mi más sincero agradecimiento a mi tutor, Dr. Jorge Otero-Santos, por su invaluable orientación y apoyo a lo largo del análisis de datos y sus comentarios durante la redacción de esta tesis. Un agradecimiento especial también a mi co-tutor y PI, Dr. Iván Agudo, por las discusiones enriquecedoras durante el transcurso de este trabajo y por brindarme la oportunidad de formar parte de esta investigación.

Este trabajo ha sido posible gracias a la beca JAE Intro, otorgada por el CSIC y financiada por el Programa Severo Ochoa, que me permitió realizar este estudio en el Instituto de Astrofísica de Andalucía. Estoy profundamente agradecido por esta oportunidad.

También me gustaría extender mi agradecimiento a los miembros del comité y al profesorado de la Universidad de Granada que dedicarán su tiempo a leer y evaluar mi tesis.

Finalmente, quiero agradecer a mis padres, hermana y gato por su apoyo durante mi tiempo estudiando el Máster en Física y Matemáticas en la Universidad de Granada.

Contents

Resumen

BL Lacertae (BL Lac), ubicado a un corrimiento al rojo z = 0.069, fue el primer blazar descubierto: un núcleo galáctico activo con un jet relativista orientado hacia la Tierra. Desde su descubrimiento, ha sido uno de los blazares más estudiados en todo el espectro electromagnético. Actualmente, la incorporación más reciente a nuestras capacidades observacionales es el *Large-Sized Telescope Prototype* o LST-1, el primer telescopio del Observatorio *Cherenkov Telescope Array*, diseñado para la observación de rayos gamma de muy alta energía a partir de los 100 GeV y hasta unos pocos TeV. En esta tesis, se estudia un evento de erupción de BL Lac durante el período de septiembre a noviembre de 2022 desde una perspectiva multibanda, incorporando datos de rayos gamma de muy alta energía del LST-1. En particular, se analizan las curvas de luz en todo el espectro y la distribución espectral de energía del blazar durante este evento, con el objetivo de proporcionar una interpretación física de los datos respaldada por modelos de emisión de jets relativistas en fuentes astrofísicas. El análisis de los datos observacionales incluye el uso de datos multibanda y la pipeline de análisis de datos del LST-1. Se analizan las correlaciones en todo el espectro y la variabilidad intra-nocturna de BL Lac, obteniéndose tiempos de duplicación del flujo. Posteriormente, se utiliza la relación de causalidad para obtener límites superiores al tamaño de las regiones de emisión. Se encontró que un modelo leptónico de emisión auto-sincrotrón Compton de dos zonas para el jet relativista concuerda con las observaciones, de acuerdo con el análisis de correlación, y se realizó un ajuste del modelo de emisión para la distribución espectral de energía en todo el espectro electromagnético del evento de erupción.

Abstract

BL Lacertae (BL Lac), located at redshift z = 0.069, was the first discovered blazar: an active galactic nucleus with a relativistic jet oriented towards Earth. Since its discovery it has been one of the most studied blazars across the complete electromagnetic spectrum; presently, the latest addition to our observational capabilities is the Large-Sized Telescope Prototype or LST-1, the first telescope of the Cherenkov Telescope Array Observatory for the observation of very-high-energy gamma-rays above energies of 100 GeV and up to a few TeV. In this thesis we study a flare event of BL Lac during September to November 2022 from a multiwavelength perspective and incorporating very-high-energy gamma-ray data from LST-1. In particular, we study the light curves across the spectrum and the spectral energy distribution of the blazar during this event, to then provide a physical interpretation of the data supported by emission models of relativistic jets in astrophysical sources. The analysis of the observational data encompasses the use of multiwavelength data and the LST-1 data analysis pipeline. The correlations across the spectrum and the intra-night variability of BL Lac are analyzed, and doubling-flux times of the variability are obtained. The causality relation is then used to obtain upper bounds to the size of the emission regions. A leptonic two-zone synchrotron self-Compton emission model for the relativistic jet was found to match with the observations, in agreement with the correlation analysis, and a fit to the emission model was performed for the broadband spectral energy distribution of the flare event.

1 | Introduction

This thesis explores the field of Very-High-Energy (VHE, E > 100 GeV; see Table 1.1) gamma-ray Astronomy, focusing on the study of Active Galactic Nuclei (AGN) and, in particular, the blazar BL Lacertae. The introduction begins with an overview of VHE gamma-ray astronomy, tracing the historical development that has made possible to detect and analyze these high-energy phenomena. Following this, the discussion centers on AGN, the energetic cores of galaxies powered by supermassive black holes (SMBHs), which are prolific sources of gamma-ray emissions. The blazar subclass, exemplified by BL Lacertae, is highlighted due to its unique orientation, where its relativistic jet points almost directly towards Earth, making it an ideal candidate for VHE gamma-ray studies. The final part of the introduction delves into the multiwavelength approach to astrophysics, which is crucial for understanding the complex processes occurring in AGN. This includes a detailed examination of the Spectral Energy Distribution (SED) model and the gamma-ray emission mechanisms that dominate at VHEs. This sets the stage for the in-depth analysis of the 2022 flaring event of BL Lacertae presented in this thesis.

1.1 Very-High-Energy Gamma-Ray Astronomy

The history of gamma-ray detection began in the early 20th century when Paul Villard identified gamma radiation as a form of highly penetrating electromagnetic radiation distinct from alpha and beta particles (Gerward, 1999). However, the field truly advanced during the mid-20th century with the development of nuclear detection technology, such as Geiger-Müller counters and scintillation detectors. These tools were initially used in nuclear physics but later laid the groundwork for detecting gamma-rays of astrophysical origin. The launch of satellites like NASA's Orbiting Solar Observatory (OSO) series in the 1960s (Paxton & Anderson, 1992) marked the

first attempts to detect gamma-rays from space. A breakthrough came with the Vela satellites in 1967, which, while monitoring for nuclear explosions, serendipitously discovered gamma-ray bursts (GRBs; Klebesadel et al., 1973), unveiling the potential of gamma-ray astronomy. Ground-based gamma-ray detection also saw substantial progress with the introduction of Cherenkov detectors in the 1970s and 1980s.

VHE gamma-ray astronomy has emerged as a vital branch of astrophysics, focusing on the study of gamma-rays with energies above 100 GeV, dramatically expanding our understanding of the most energetic processes in the Universe. This includes phenomena such as supernova remnants (SNRs), pulsar wind nebulae (PWNe), and, most notably, AGN with relativistic jets. In the context of blazar emissions (see Section 1.3.1), initial insights were obtained through coordinated observational campaigns in the 1990s, using instruments like the Compton Gamma-Ray Observatory (Gehrels et al., 1994) and the Rossi X-ray Timing Explorer (Bradt et al., 1993). These campaigns, which combined data from radio to gamma-rays, revealed that blazar emissions are often dominated by Compton scattering in the gamma-ray band (Hartman et al., 1992). However, the limited sensitivity of early instruments restricted the scope of these studies. The launch of the *Fermi*-LAT satellite in 2008 (Atwood et al., 2009) and still in operation marked a turning point, significantly expanding the number of detected gamma-ray blazars (detecting 7194 gamma-ray sources of which the vast majority are blazars, Ballet et al., 2023), and enabling more extensive multiwavelength studies (Massaro et al., 2009). The advent of ground-based Imaging Air Cherenkov Telescopes (IACTs), which observe the Cherenkov radiation produced when gamma-rays interact with the Earth's atmosphere, such as the High Energy Stereoscopic System (HESS), the Major Atmospheric Gamma Imaging Cherenkov (MAGIC) telescopes, and the Very Energetic Radiation Imaging Telescope Array System (VERITAS), has further increased the detection of VHE gamma-ray blazars, allowing for a more comprehensive understanding of their spectral energy distributions and variability (Ribó, 2008; Acciari et al., 2020). Recent advancements in VHE gamma-ray astronomy are epitomized by the development of the Cherenkov Telescope Array Observatory (CTAO), which aims to significantly enhance our observational capabilities. The Large-Sized Telescope Prototype (LST-1), featuring a 23-meter diameter dish and designed to detect gamma-rays in the energy range from 20 GeV to 3 TeV, is the first operational telescope of the CTA, providing unprecedented sensitivity and resolution for observing VHE gamma-rays (CTA Consortium, 2019).

Observations of VHE gamma-rays are crucial for understanding the mechanisms driving emission in extreme environments as is in the case of blazars. These observations allow us to probe the physical processes at play, such as particle acceleration and in-

teractions in relativistic jets. Multiwavelength observations, combining VHE gamma-rays with data from other bands of the electromagnetic spectrum, are particularly valuable for providing a comprehensive picture of these energetic sources. For blazar observations, pushing the observable energy threshold in the VHE gamma-ray band towards ~ 20 GeV is particularly important as most of the blazars show soft spectra in the VHE gamma-ray range (Hovatta & Lindfors, 2019).

Name	Approximate Energy Range
Low Energies (LE)	0.5 - 30 MeV
High Energies (HE)	30 MeV - 100 GeV
Very High Energies (VHE)	100 GeV - 100 TeV
Ultra High Energies (UHE)	100 TeV - 100 PeV
Extremely High Energies (EHE)	> 100 PeV

Table 1.1: Energy ranges of of the different domains within gamma-ray astronomy.

Gamma-rays in the VHE domain are emitted by a variety of astrophysical sources. These include pulsars, which are rapidly rotating neutron stars with strong magnetic fields (Browning et al., 1971); PWNe, where the wind from a pulsar interacts with surrounding material (Bednarek & Bartosik, 2003); and SNRs, the remnants of massive stars after they explode (Funk, 2008). Other sources are gamma-ray binaries, systems consisting of a compact object and a massive star (Adams et al., 2021); novae, explosive events in binary systems involving a white dwarf (Abdo et al., 2010a); star-forming regions; and the Galactic Centre, a steady source of gamma-rays (Albert et al., 2006). Extragalactic sources include AGN, particularly blazars (Aleksić et al., 2012), and starburst galaxies with high star formation rates (VERITAS Collaboration et al., 2009). Additionally, GRBs, which are intense and short-lived extragalactic events, also emit gamma-rays in this energy range (MAGIC Collaboration et al., 2019a).

1.2   Active Galactic Nuclei

AGN are some of the most luminous and energetic objects in the Universe, theorized to result from the accretion of matter onto SMBHs at the centers of galaxies. They exhibit a wide range of phenomena, including the emission of relativistic jets, which are collimated beams of particles accelerated to near-light speeds. These jets can produce radiation across the entire electromagnetic spectrum, from radio waves to gamma rays.

The study of AGN began in the 1940s when Carl Seyfert identified galaxies with unusually bright nuclei, now known as Seyfert galaxies. This discovery laid the groundwork for recognizing AGN as a distinct class of astronomical objects. The subsequent discovery of radio galaxies in the 1950s, emitting intense radio waves from their central regions, and in the 1960s, the identification of quasars, which outshine their host galaxies, further expanded the AGN category. Maarten Schmidt's realization in 1963 that quasar spectral lines were highly redshifted confirmed these objects as extremely distant and powerful, confirming their extragalactic nature and providing the first clear evidence of SMBHs.

The AGN Unified Model (See Fig. 1.1), developed in the late 1980s and 1990s, was a significant theoretical advancement, proposing that the diversity of AGN types (e.g., Seyfert galaxies, quasars, radio galaxies) could be explained by orientation effects and the presence of obscuring material around the nucleus (Urry & Padovani, 1995). As observational capabilities expanded, particularly with X-ray astronomy, AGN were found to be strong X-ray emitters, revealing processes occurring near the SMBH's event horizon. Today, AGN are studied across the entire electromagnetic spectrum, providing critical insights into SMBH growth, jet formation mechanisms, and the role of AGN feedback in galaxy evolution.

1.2.1   AGN Morphology

The core of an AGN is the SMBH, surrounded by an accretion disk of infalling matter. This disk is typically composed of gas and dust that spirals inward due to the immense gravitational pull of the black hole (Netzer, 2013). As the material in the disk moves inward, it heats up due to viscous dissipation and radiates across the electromagnetic spectrum, particularly in the ultraviolet (UV) and optical bands (Shakura & Sunyaev, 1973). Beyond the accretion disk lies a region known as the broad-line region (BLR), consisting of rapidly moving, hot ($T \sim 10^4$ K), high density ($n_e > 10^9 \, \mathrm{cm}^{-3}$) clouds of gas that emit broad emission lines in the AGN's spectrum (Peterson, 2006). These lines are broadened due to the Doppler effect, as the gas clouds orbit close to the black hole at high velocities ($v \sim 3 \times 10^4$ km/s). Further out, the narrow-line region (NLR) contains clouds of gas moving at lower velocities, resulting in narrower emission lines. This region colder and less dense than the BLR is illuminated by the radiation from the central engine, producing characteristic spectral lines in the optical and near-infrared bands (Peterson, 1997). Surrounding these central regions is the dusty torus, a "doughnut-shaped" structure of obscuring material that plays a crucial role in the
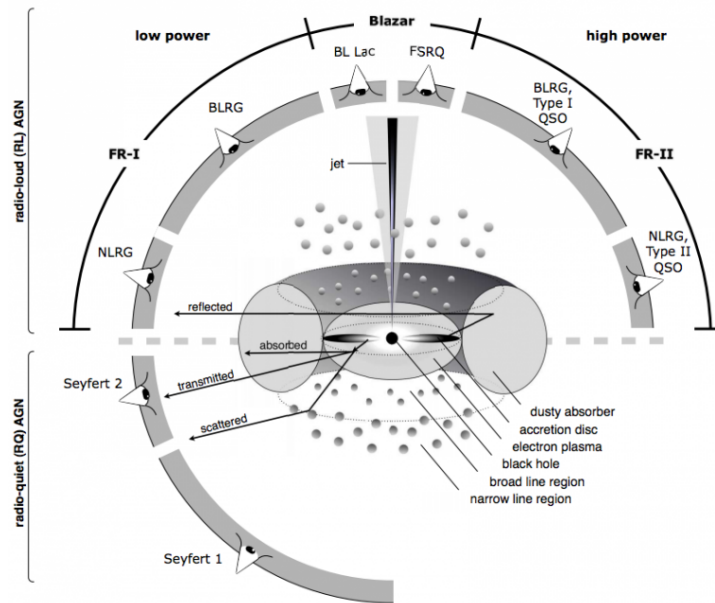
Figure 1.1: AGN Unified Model ([Beckmann & Shrader], [2012]). Different AGN types can be defined attending to differences in their radio loudness/quietness, electromagnetic power and orientation angle of the relativistic jet.

appearance of the AGN ([Netzer], [2013]). The orientation of this torus relative to our line of sight largely determines the observed properties of the AGN ([Netzer], [2015]).

1.2.2   AGN Classification

The differences in observed AGN types arise from variations in their central structure, orientation, and the presence of their jets, as can be seen in Fig. [1.1].

Radio Loud Galaxies have very weak radio emission and do not develop relativistic jets ([Wilson & Colbert], [1995]).

- *Seyfert Galaxies* are relatively low-luminosity AGN ([Seyfert], [1943]). *Seyfert 1* galaxies have both broad and narrow emission lines due to a visible BLR, typically observed face-on. *Seyfert 2* galaxies only show narrow lines, as the BLR is obscured by the dusty torus, viewed edge-on. ([Khachikian & Weedman], [1974])

- *Radio-quiet quasars* are similar to Seyfert 1 but much brighter, with weak radio emission ([Véron-Cetty & Véron], [2000]).

Radio Loud Galaxies are dominated by large-scale radio lobes powered by jets.

- *Fanaroff-Riley I* radio galaxies have jets that fade with distance, typically lower in luminosity (Blandford & Königl, 1979).

- *Fanaroff-Riley II* galaxies have bright, extended jets with prominent lobes and hotspots, associated with more powerful AGN (Wilson & Colbert, 1995).

- *Blazars* have a relativistic jet closely oriented in the direction of the Earth.

1.3 Blazars

Blazars are broadly classified into two main categories based on their optical spectral features (Urry & Padovani, 1995): *BL Lacertae* (BL Lac) objects and *flat-spectrum radio quasars (FSRQs)*. BL Lacs show very weak or even absent emission lines in their optical spectra. Their SEDs are typically dominated by non-thermal emission from the jet; however, especially in the case of FSRQs, other regions of the AGN, such as the accretion disk, dusty torus and BLR can also contribute significantly to the observed emission. FSRQs exhibit strong, broad emission lines in their optical spectra, and they generally have a more prominent thermal component in their SEDs, likely from the accretion disk and BLR. The SEDs of FSRQs usually peak at lower frequencies compared to BL Lac objects. Furthermore, blazars exhibit a characteristic double-peaked SED: one peak at lower energies, ranging from infrared to X-rays depending on the type of blazar, and another peak at higher energies in the gamma-ray range (see Fig. 1.2). The low-energy peak is typically due to synchrotron radiation, while the high-energy peak is explained by different processes, which are discussed in Section 1.3.1.

While the traditional classification of blazars separates them into BL Lac objects and FSRQs based on their optical spectral features, a newer classification known as the "blazar sequence" is based on the relationship between luminosity and the synchrotron peak frequency. In this classification, FSRQs are the most luminous and have their synchrotron peak at lower frequencies, whereas BL Lacs are less luminous and are further subdivided based on the peak frequency of their synchrotron emission into: low-frequency peaked ($\nu < 10^{14}$ Hz) BL Lacs (LBLs), intermediate-frequency peaked ($10^{14} < \nu < 10^{15}$ Hz) BL Lacs (IBLs), high-frequency peaked ($10^{15} < \nu < 10^{17}$ Hz) BL Lacs (HBLs), (Padovani & Giommi, 1995) and extreme high-frequency peaked ($\nu > 10^{17}$ Hz) BL Lacs (EHBLs; Costamante et al., 2001).
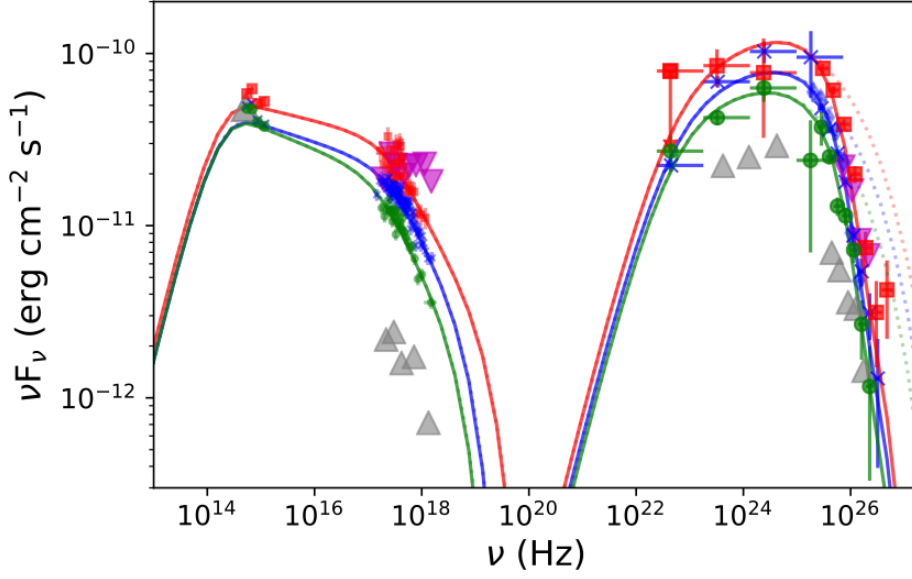
Figure 1.2: Example of a blazar SED across frequencies (x-axis in Hz, logarithmic scale) obtained from Adams et al. (2022). The y-axis (νF_ν in erg cm^{-2} s^{-1}) represents the energy flux per unit area. The blue (cross), red (square) and green (circle) markers represent flare activity of the blazar VER J0521+211 for three different periods of time during 2013 and 2014, using data from *Swift*-UVOT, *Swift*-XRT, *Fermi*-LAT, MAGIC and VERITAS. The solid curves represent a one-zone synchrotron self-Compton model.

Blazars are known for their large and typically unpredictable variability across the electromagnetic spectrum. This variability can manifest on a wide range of timescales, from minutes to years. Studying this variability is one of the most direct methods to gain insights into their emission mechanisms and jet morphology (Wagner & Witzel, 1995). The fastest observable variability can be used to place constraints on the size of the emission regions responsible for this variability, using the causality condition (Aharonian et al., 2007), which is given by

$$R < c\frac{\delta_D \Delta t}{(1+z)}, \tag{1.1}$$

where R is upper bound of the size of the emitting region, Δt is the observed variability timescale, δ_D is the Doppler factor of the jet, i.e. the factor of relativistic boosting of the emission, c is the speed of light, and z is the redshift of the blazar.

1.3.1 Emission Processes

The emission from blazars is dominated by processes occurring in their relativistic
jets. Low-energy emission is dominated by synchrotron radiation. For gamma-rays,
the models are classified into leptonic and hadronic models. Leptonic models are the
most commonly considered because they successfully explain many observed features
of blazars. In rarer circumstances, since AGN are candidates for extragalactic neutron
emission, interactions involving relativistic protons, such as proton synchrotron ra-
diation or photopion production, may also contribute to the high-energy emission. In
hadronic models, neutral pions produced in p-p collisions and p-γ interactions decay
into photons, contributing to the observed gamma-ray emission. However, given that
these events are very rarely detected, in this work we will focus on leptonic models.
These and further alternative emission models are discussed in Blandford et al. (2019).

Synchrotron Radiation

Synchrotron radiation is the primary mechanism responsible for the low-frequency
peak of the SED (Konigl, 1981). It occurs when relativistic charged particles, typically
electrons, spiral around magnetic field lines at nearly the speed of light (see Fig. 1.3).
The acceleration of these charged particles produces electromagnetic radiation, which
is emitted in a narrow cone in the direction of the particle's motion. The power radi-
ated by a single electron in a magnetic field B can be described as

$$P = \frac{2}{3} \left(\frac{e^4}{m_e^2 c^3} \right) \gamma^2 B^2, \tag{1.2}$$

where e is the charge of the electron, m_e is the mass of the electron, and $\gamma = \left(1 - v^2/c^2\right)^{-1/2}$
is the Lorentz factor representing the relativistic effects on the electron, where v is the
speed of the electron and c the speed of light. The frequency of the emitted radiation
is primarily determined by the electron's energy and the magnetic field strength. The
critical frequency ν_c at which most of the synchrotron power is emitted is given by

$$\nu_c = \frac{3}{2} \left(\frac{e}{2\pi m_e c} \right) \gamma^2 B. \tag{1.3}$$

Although leptons are typically assumed, any charged particle could, in principle, un-
dergo synchrotron radiation. Since synchrotron emission is intrinsically polarized,
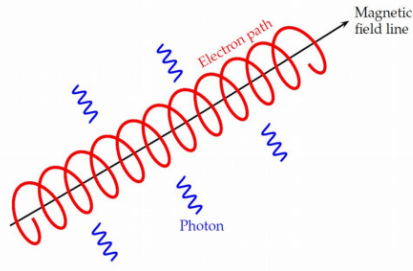
Figure 1.3: Visual representation of synchrotron radiation (Richmond, 2024).

the polarization of radio to X-ray emissions is another key characteristic of blazars, providing valuable information about the magnetic field, the jet, and its structure.

Inverse Compton Scattering

Inverse Compton (IC) scattering is responsible for the high-energy emission. It occurs when relativistic electrons scatter low-energy photons to higher energies. The seed photons can be either the synchrotron photons themselves (synchrotron self-Compton, SSC; Maraschi et al., 1992) or external photons from the accretion disk, BLR, or dusty torus (external Compton, EC; Dermer & Schlickeiser, 1993). This latter process is particularly relevant in FSRQs, where these components are prominent, while in BL Lacs, these regions are often weak or even absent.
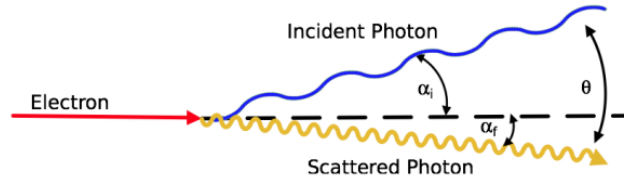
Figure 1.4: Visual representation of IC scattering (Ertley, 2014).

The energy gained by the photon after the scattering (see Fig. 1.4) is described in terms of its wavelength as (Rybicki & Lightman, 1979):

$$\Delta\lambda = \lambda_f - \lambda_i = \lambda_C(1 - \cos\theta), \tag{1.4}$$

where λ_i and λ_f are respectively the wavelengths of the incident and scattered photons, θ is the angle between them, and λ_C is the Compton wavelength, defined as $\lambda_C = \frac{h}{mc} = 0.02426\,\text{Å}$ for electrons.

1.3.2 Absorption Processes: Extragalactic Background Light (EBL)

The gamma-ray emission from distant blazars is attenuated by the Extragalactic Background Light (EBL), which consists of low-energy background photons in IR, optical, and UV wavelengths (Gould & Schréder, 1966). These photons interact with gamma-rays, leading to their annihilation via pair production, particularly at energies greater than 10 GeV (Vassiliev, 2000). The observed gamma-ray spectral flux differential is attenuated as a function of energy and redshift, described by an optical depth $\tau(E, z)$ as the rate of exponential decay,

$$\left(\frac{d\phi}{dE}\right)_{\text{observed}} = \left(\frac{d\phi}{dE}\right)_{\text{intrinsic}} \cdot e^{-\tau(E,z)}. \tag{1.5}$$

This optical depth depends on the photon density distribution of the EBL and the cross-section of pair production interactions, the latter being larger for photons of higher energies. Therefore, gamma-ray photons of the highest energies are more like to be attenuated. Similarly, the attenuation becomes more severe for distant sources.

1.4 BL Lacertae

BL Lacertae (BL Lac), located at a redshift of $z = 0.069$ (Miller et al., 1978), was the first discovered BL Lac object and serves as the prototype for BL Lac objects, lending its name to the entire class (Schmidt, 1963). It is one of the most studied and monitorized blazars, and one of the more than 90 known blazars known to emit VHE gamma-rays. BL Lac is a highly variable source, exhibiting significant changes in brightness across its emission spectrum. This variability is often associated with flares, during which the brightness of the blazar can increase dramatically over short periods. The study of BL Lac and other blazars is essential for understanding the physical processes within relativistic jets. These jets are believed to be powered by the accretion of material onto the supermassive black hole and the subsequent release of energy through magnetic reconnection and shock acceleration (Agarwal et al., 2023). Observations of flares in blazars, such as those from BL Lac, provide valuable data for testing theoretical models of jet acceleration. In the rest of this thesis, the focus will be on studying the flare of BL Lac in 2022, which, along with another in 2021, is one of the brightest ever detected from this source.

2 | Observations

This chapter details the observational procedures and analyses carried for the monitoring of BL Lacertae with a focus on VHE gamma-ray data using the Large-Sized Telescope Prototype (LST-1). We begin by describing the Cherenkov Technique, which is the cornerstone method for detecting VHE gamma-rays. Following this, we provide an overview of the LST-1, outlining its capabilities and role in capturing the data critical to this study. The subsequent section on LST-1 data analysis discusses the methodologies applied to process and analyze the collected data. As part of the data validation process, observations of the Crab Nebula — the standard candle in VHE gamma-ray astronomy — were used as a reference to verify the accuracy of the LST-1's performance. Finally, we introduce the multiwavelength data obtained from additional observational instruments that complement the VHE gamma-ray data.

2.1 VHE gamma-rays: LST-1

2.1.1 Cherenkov Technique

The Cherenkov technique, specifically utilized in Imaging Atmospheric Cherenkov Telescopes (IACTs) such as LST-1 and its predecessors, is designed to detect VHE gamma-rays from cosmic sources by capturing the faint Cherenkov light emitted by particle showers initiated when these gamma-rays interact with Earth's atmosphere. The technique leverages the properties of Cherenkov radiation (Cherenkov, 1934), which occurs when charged particles move faster than the speed of light in a given medium (in this case, the Earth's atmosphere).

When a gamma-ray enters the Earth's atmosphere, it interacts with the atmospheric nuclei through pair production and subsequent cascading processes. This interaction

produces an extensive air shower, a cascade of rapidly multiplying secondary particles as they travel through the atmosphere.

However, cosmic rays — discovered by Victor Hess in 1912 (Hess, 1912; Millikan, 1926), mainly composed of protons (∼89%), alpha particles (helium nuclei, ∼9%), electrons and positrons (∼1%), heavier nuclei (C, N, O, Fe, ∼1%), and neutrons, neutrinos and gamma-rays (∼0.1%) — can also interact with atmospheric nuclei leading to similar particle showers. Hence, we identify three possible types of cascades depending on the primary particle (Rao & Sreekantan, 1998, see Fig. 2.1):

- **Electromagnetic Shower**: Triggered by a high-energy photon interacting with atmospheric nuclei, leading to the creation of an electron-positron pair. These particles share the photon's energy and interact with the atmosphere, emitting lower energy photons through Bremsstrahlung. This process repeats, creating a cascade of particles until the energy of the positrons falls below a critical threshold of 85 MeV. This occurs when the radiative energy loss of the secondary particles exceeds that from the Bremsstrahlung process.

- **Hadronic Shower**: Occurs when a cosmic ray interacts with the atmosphere, creating various particles like pions and kaons. Neutral pions can decay into photons, contributing to electromagnetic subshowers. The hadronic shower continues until the energy of pions drops below a critical level. These showers are broader, more irregular, and produce a richer variety of secondary particles compared to electromagnetic showers (see Fig. 2.1). These cascades are the most significant contribution to the observed gamma-ray background.

- **Electron Shower**: Initiated by an electron, resulting in a cascade similar to the electromagnetic shower, where the products are only photons, electrons, and positrons. These showers are significant in background detection and are challenging to distinguish from electromagnetic showers.

The secondary charged particles in the shower, particularly relativistic electrons and positrons, travel through the atmosphere at velocities exceeding the speed of light in air. This superluminal motion causes the emission of Cherenkov radiation — a coherent burst of light emitted in a narrow cone around the direction of the particle.

When a charged particle moves faster than the speed of light in the medium, it polarizes the medium, leading to the emission of Cherenkov light (Cherenkov, 1934) at a
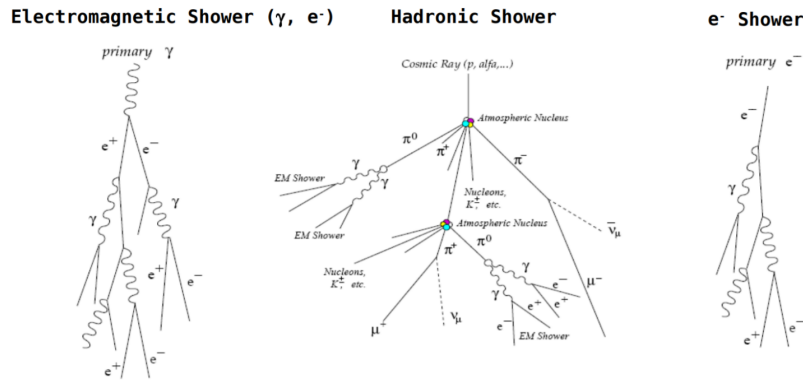
Figure 2.1: Schemes for electromagnetic, hadronic, and electron showers. Obtained from López-Oramas (2015).

characteristic angle θ, which can be calculated as $\cos\theta = \frac{1}{\beta n}$. Here, $\beta \approx 1$ for relativistic particles, and the refractive index of Earth's atmosphere $n \approx 1.00029$. This gives an emission angle of about 1.3°. The resulting Cherenkov light propagates with a wavelength of approximately 350 nm. The Cherenkov light's footprint on the ground typically has a radius of about 150 m at an altitude of 2000 meters.

IACTs are specialized telescopes designed to detect Cherenkov radiation by imaging the Cherenkov light (Cherenkov, 1934) pool created by the air showers. The key technique used in the analysis of these images is the Hillas parametrization, which involves characterizing the shape and orientation of the Cherenkov light image on the camera (see Fig. 2.2). This method reduces the complex shower image into a set of parameters such as width, length, and orientation, crucial for reconstructing the direction and energy of the primary gamma-ray (Hillas, 1985). The CTAO utilizes this parametrization to optimize the discrimination between gamma-ray and cosmic-ray-induced showers. By analyzing the geometrical properties of the image, the Hillas parameters help to distinguish between different types of events, enabling the detection of gamma-rays from astrophysical sources (CTA Consortium, 2019).

2.1.2   The Large-Sized Telescope Prototype (LST-1)

The Large-Sized Telescope Prototype (LST-1) is a cutting-edge prototype for the LST series, developed as part of the CTAO, the next-generation facility for VHE gamma-ray astronomy. The CTAO will feature two arrays, one in each hemisphere, equipped with telescopes of various sizes to cover an energy spectrum from tens of GeV to
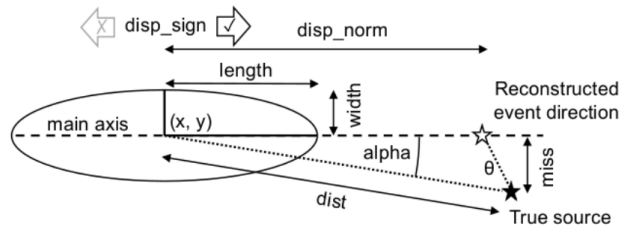
Figure 2.2: Scheme of Hillas parametrization of a shower image, obtained from Abe et al. (2023a). These parameters are used to reconstruct the observation events.

Figure 2.3: The LST-1 at the Observatorio Roque de los Muchachos. Credit: Tomohiro Inada (LST Collaboration).

over 100 TeV. The LST-1, specifically designed and optimized to detect gamma-rays in the 20 GeV to 150-200 GeV range, is located at the Observatorio del Roque de los Muchachos on La Palma, Canary Islands, Spain.

The LST-1 has been operational since November 2019, focusing on the lowest energy range of the VHE gamma-ray band. Standing 45 m tall and weighing 100 tonnes, the LST-1 is engineered for rapid repositioning within 20 s to capture transient events. The reflective system consists of a parabolic segmented dish with 198 mirrors, with a diameter of 23 m, covering an area of 368 m^2, and with a focal length of 28 m. The dish is coupled with a highly pixelized camera based on photomultiplier tubes (PMTs), designed to capture and convert Cherenkov light into digital signals, with 1855 pixels of 0.1° imaging size and a field of view (FoV) of 4.3° (CTA-LST Project, 2019).

The LST-1 typically operates in the so-called wobble mode (Fomin et al., 1994), an observational technique commonly employed by IACTs, developed with the aim of reducing the observing time needed to record both the signal of the source and the surrounding background. In this mode, the telescope is pointed slightly off-axis from the target source, typically by 0.4° from the center of the camera's FoV. This displacement allows the telescope to observe both the source (ON region) and the surrounding background (OFF region) within the same observational run. The position of the source is shifted every ∼20 minutes to different parts of the camera, ensuring consistent sensitivity while simultaneously capturing background data. Typically, reflected positions of 90, 180 and 270 degrees with respect to the position of the source are used for background extraction. This technique improves the accuracy of background estimation and reduces systematic errors by using the same camera pixels for both the source and background measurements.

2.1.3   LST-1 Data Analysis

Data analysis of LST-1 is a complex, multi-stage process designed to handle the large volumes of data generated, ensuring accuracy and efficiency from raw data to final scientific products. It is divided into several Data Levels: R0 for raw data, R1 for calibrated data, DL1 A/B for reconstructed event parameters, DL2 for selected gamma-like events, DL3 for associated instrument response functions, DL4 for reduced spectrum datasets, and DL5 for final spectral and temporal analysis products. Data Storage involves high-capacity storage arrays and databases that provide both short-term storage for real-time processing and long-term archival solutions for the different data levels. The low level analysis steps (pre-DL3 level) is performed with the `cta-lstchain` software package, developed in the PYTHON programming language (López-Coto et al., 2022). The high level analysis (post-DL3 level) involves the usage of the `gammapy` PYTHON package, a set of tools developed specifically to deal with high-energy gamma-ray astronomy data (Donath et al., 2023). This subsection contains a summary of the low level data preprocessing and the high level data analysis we performed for the data corresponding to the flare period of BL Lac.

Low Level Analysis (Pre-processing):

The Data Acquisition System (DAQ) is the initial stage of the pipeline, capturing raw data directly from the LST-1. This system comprises custom-designed electronics and software that interface with the sensors of the telescope. The primary function of

the DAQ system is to digitize the analog signals from PMTs. The raw data (R0) are calibrated to correct for instrumental effects, resulting in R1 data. Some data volume reduction is performed and some metadata is associated, resulting in DL0. These data are then subjected to pixel-wise charge integration, producing DL1 A data.

Subsequent steps include image cleaning to filter out noise, and image parameterization to extract key features, resulting in DL1 B data, and then application of random forest models trained on Monte Carlo (MC) simulations to identify gamma-like events, progressing from DL1 B to DL2 datasets. This includes the reconstruction of energy of the primary shower particle, the reconstruction of the direction, and gamma/hadron classification. The gammanness parameter is defined, indicating the probability a primary shower particle is a gamma-ray or hadron noise.

Selection of gamma-like events is a critical phase, ensuring that only high-confidence gamma-ray events are retained. This step is particularly important because, in Cherenkov telescopes, for every true gamma-ray trigger, approximately $\sim 10^4$ noise triggers from cosmic ray-induced air showers are generated. Therefore, accurately distinguishing and discarding these background events is essential for the integrity of the data analysis. Energy-dependent selection cuts are applied to distinguish gamma-ray events from the background, resulting in a refined list of observed gamma-like events. We use energy dependent cuts to optimize the number of events selected for each energy, since sensitivity and performance of LST-1 vary across its energy range of observation. Throughout this thesis we have used cuts with 90% efficiency for gammaness. Instrument response functions (IRFs) are then generated and associated with these event lists, forming the DL3 data files.

The production of IRFs, which provide conditional probabilities of detection of gamma-rays, involves sophisticated interpolation techniques based on the performance and reponse of the telescope in a set of positions in the sky along a declination line in the sky. This is to account for varying observational conditions depending on the telescope. Therefore, factors such as air mass coverage and geomagnetic field effects are considered to produce accurate IRFs.

High Level Analysis:

High-level analysis using the `gammapy` PYTHON package allows for the detailed examination of the LST-1 data. In this thesis the final science products (DL5) produced from the LST-1 data pipeline will be the SEDs and light curves (LCs) of the BL Lac event flare. We have also analyzed the Crab Nebula during a similar period as a san-

ity check of the analysis. This is because this source is known for being the standard candle in VHE gamma-ray astronomy. The starting point for the high level analysis are the DL3 files. The DL3 files of gamma-like events are reduced into DL4 binned data using the `makers gammapy` module, and likelihood fitting is performed on the DL4 data to generate the SEDs and LCs using the modeling and estimators gammapy modules, as detailed below.

For the BL Lac observations used in this thesis, the LST-1 operated in a standard wobble mode (4 wobbles at positions 0, 90, 180 and 270 deg and 0.4 deg offset), accumulating ~53 hours of data over 30 nights between MJD 59843 to MJD 59909 (September 16th to November 21st 2022). After applying standard data quality cuts to account for atmospheric transmission, clouds, moonlight and other effects that may impact the quality of the data, ~36 hours of data were selected, with an energy threshold of 100 GeV. Significant VHE gamma-ray activity was detected, particularly on the nights of October 20-21 and November 13-14, 2022. BL Lac results are presented in Chapter 3.

For the Crab Nebula the period of observation used are the eight nights from MJD 60289 to MJD 60297 (December 11th 2023 to December 19th 2023). The results on the Crab Nebula are presented below (see Fig. 2.5) as examples of the data products and as sanity checks for the analysis.

Theta squared plots

Theta squared (θ^2) plots are histograms that display the distribution of ON and OFF counts as a function of the squared angular distance from the source position. These plots are used to evaluate the expected signal excess from a source for θ^2 values close to 0. We use them to assess whether a source has been significantly detected or not. In VHE gamma-ray astronomy, a detection is typically defined as a signal with a significance of at least 5 sigma (5σ) relative to the background. This significance is calculated using equation (17) from Li & Ma (1983):

$$\sigma = \sqrt{2} \left\{ N_{\mathrm{ON}} \ln \left[\frac{1+\tau}{\tau} \left(\frac{N_{\mathrm{ON}}}{N_{\mathrm{ON}} + N_{\mathrm{OFF}}} \right) \right] + N_{\mathrm{OFF}} \ln \left[(1+\tau) \left(\frac{N_{\mathrm{OFF}}}{N_{\mathrm{ON}} + N_{\mathrm{OFF}}} \right) \right] \right\}^{1/2} \quad (2.1)$$

where τ is the ratio of the OFF/ON exposure, and N_{ON} and N_{OFF} the number of detected ON and OFF events.. This method allows us to determine the significance of a potential gamma-ray signal from the source.

For the Crab Nebula, a total of 30 runs were selected, with a cumulative observing time of 8.5 hours, using 2 wobbles. The θ^2 plot for the Crab Nebula, such as shown in Fig. 2.4, demonstrates the signal significance derived from these observations. We consider a standard θ^2 cut for extracting the signal from our source of $\theta^2 < 0.04 \, \mathrm{deg}^2$. The same data selection criteria were applied to the BL Lac observations.

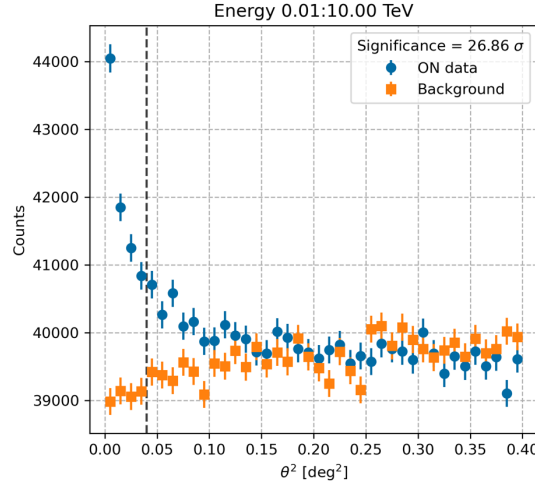Figure 2.4: θ^2 plot for the Crab Nebula for night MJD 60295 to MJD 60296, for total observing time of 2.69h. The ON and OFF distributions are shown, with the background normalized using the ratio of counts in the radial range $[0.1, 0.4] \, \mathrm{deg}^2$ and showing a significance cut at $\theta^2 = 0.04 \, deg^2$. The signal significance is calculated using the formula from Li & Ma (1983).

SED and LC generation

We conduct one-dimensional spectral analysis along the energy axis, using the ON-OFF forward folding method: this consists of assuming a spectral shape, starting with a Power Law, and fitting the observed data to this model while accounting for the background using the OFF data. This method allows for an accurate estimation of the source spectrum by considering both the signal and background simultaneously.

For the present analysis we use an energy axis that spans from 0.01 to 10 TeV, divided into ten bins per decade (i.e., order of magnitude), providing a fine resolution across a wide energy range. To generate the SED, we apply the same selection masks used for the θ^2 plots, ensuring consistency in event selection criteria. Additionally, we impose

a minimum livetime requirement of 30 seconds per run to ensure that the data quality is sufficient for reliable spectral analysis.

First, we determine the pivot (decorrelation) energy for a Power Law spectral model

$$\phi(E) = \phi_0 \cdot \left(\frac{E}{E_0} \right)^{-\Gamma}, \tag{2.2}$$

where Γ is the spectral index, ϕ_0 the normalization flux, and E_0 the normalization energy; the latter serves as the reference normalization energy for the LogParabola model that will be used as final model for the spectrum and SED. This definition of the pivot energy is crucial as it minimizes the correlation between the spectral parameters, leading to a more robust fit. Then, the spectrum is fitted with a LogParabola function with the estimated pivot energy, written as

$$\phi(E) = \phi_0 \cdot \left(\frac{E}{E_0} \right)^{-\alpha - \beta \log\left(\frac{E}{E_0} \right)}. \tag{2.3}$$

where E_0 is the normalization energy, and α and β fit parameters. This expression refers to the observed — therefore absorbed — gamma-ray spectrum, before correcting the attenuation introduced by the EBL. This correction will ultimately be applied for modeling the intrinsic broadband emission of the source (see Section 3.3).

Following this, we utilize the `FluxPointsEstimator` to compute the flux points after fitting the LogParabola model. This estimator calculates the differential flux in the case of the spectrum (differential energy spectrum, DES; $\frac{d\phi}{dE}$) or the energy flux in the case of the SED, at different energy bins, providing a detailed description of the source's spectrum and SED. The computed flux points are then used to generate the SED (expressed as $E^2 \cdot \frac{d\phi}{dE}$), which visually represents how the energy output of the source varies with energy. The reconstructed SED of the Crab Nebula is shown in Fig. 2.5 as an example.

Finally, we employ the `LightCurveEstimator` to generate the LC performing the flux integral $\int_{E_{\min}}^{E_{\max}} \frac{d\phi}{dE} \cdot dE$. This involves dividing the observation period into temporal bins and fitting the spectral model within each bin to observe variations in the source's flux over time. The LC is an essential tool for understanding the temporal behavior of the source, such as detecting flares, variability, or long-term trends. The reconstructed LC of the Crab Nebula is shown in Fig. 2.5 as an example.
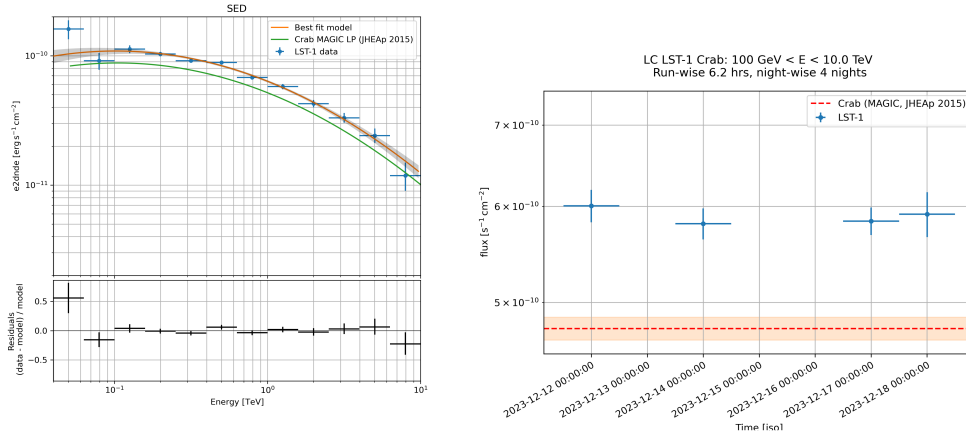
Figure 2.5: *Left:* Crab Nebula SED. Spectral points are represented with blue dots and the best fit is shown in orange. Residuals are shown at the bottom panel. *Right:* Crab Nebula LC from December 11th to 19th 2023, for an observing time of 6.2 hours. For reference, the SED and flux measured by MAGIC (Aleksić et al., 2015) are also shown.

2.2 Multiwavelength Data

Multiwavelength LC and SED data of BL Lac for the same period were also obtained. While the LST-1 measures energies from 20 GeV to 3 TeV, data for lower energies proceed from a number of sources detailed below and provided already reduced.

2.2.1 High-Energy Gamma-Rays: *Fermi*-LAT

Launched in 2008, the *Fermi Gamma-ray Space Telescope,* and specifically its Large Area Telescope (LAT), is a pioneering space-based observatory designed to observe the Universe in the HE gamma-ray band. Positioned in low Earth orbit, it covers an energy range from 20 MeV to over 300 GeV, with its best sensitivity up to a few GeV, detecting some of the most energetic phenomena in the cosmos (Atwood et al., 2009).

2.2.2 X-Ray Observations: *Swift*-XRT

The *Swift X-Ray Telescope (XRT)* is a space-based telescope, part of NASA's *Swift* mission since 2004. It observes the X-ray band from 0.2 to 10 keV (Burrows et al., 2004).

In the context of the BL Lac observations, we obtained X-ray LCs from the XRT in the same period as LST-1's observations, which are vital for examining the medium-energy emission. This data helps bridge the gap between optical/UV and gamma-ray observations, offering a more complete view of the emission mechanisms.

2.2.3   Ultraviolet-Optical Observations: *Swift*-UVOT

The *Ultraviolet/Optical Telescope (UVOT)*, also aboard the *Swift* satellite, complements the XRT by covering the optical-UV range. Since its launch in 2004, *Swift*-UVOT has been providing high-cadence observations of the UV and optical counterparts of X-ray sources (Roming et al., 2005). UVOT is particularly valuable for its ability to capture simultaneous data across multiple bands, aiding in the construction of broad SEDs. BL Lac observational data was obtained for the filters (Poole et al., 2008) *vv* (5468 Å), *bb* (4392 Å), *uu* (3465 Å), *w1* (2600 Å), *m2* (2246 Å), *w2* (1928 Å).

2.2.4   Optical Observations

Optical observations were obtained for several observatories and facilities listed below. The data were already corrected for the contribution to the total emission of the host galaxy (Nilsson et al., 2007), leaving only the contribution of the relativistic jet; and corrected from the Galactic extinction (Schlafly & Finkbeiner, 2011).

Zwicky Transient Facility (ZTF):   Operational since 2018, the *Zwicky Transient Facility (ZTF)* is a cutting-edge optical survey telescope at the Palomar Observatory, California. It was designed to survey the northern sky with an unprecedented speed, using its wide FoV to capture transient and variable sources in optical wavelengths (Bellm et al., 2019). We retrieve BL Lac observations in v and r Sloan bands, later converted to the R and V Johnson-Cousins filters as the rest of the data.

Turku University Observatory: The *Turku University Observatory* in Finland operates telescopes in the B, V, and R optical bands (400-700 nm). For the BL Lac observations, we obtained R band LCs from the Turku Observatory as part of the Tuorla blazar monitoring programme (Takalo et al., 2008), in which a large list of blazars is regularly observed with the aim of constructing long-term optical LCs with which to study blazar variability (Nilsson et al., 2018).

Las Cumbres Observatory (LCOGT): LCOGT is a global network of robotic telescopes that operates in the optical band of the spectrum (Brown et al., 2013). In the context of the BL Lac observations, LCOGT contributed LCs with the V, and R bands. The global distribution of LCOGT telescopes ensures that we can observe BL Lac continuously, regardless of local day-night cycles.

IAC80 Telescope: Located at the Teide Observatory in the Canary Islands, Spain, it has been operational since 1991. For the BL Lac observations, we obtained LCs in the B, V, R and I bands (400-700 nm) from the IAC80.

Sierra Nevada Observatory (OSN): Operated by the Instituto de Astrofísica de Andalucía (IAA), it is located in Andalusia, Spain. The observatory consists of two telescopes, one with a 90 cm aperture and the other with a 150 cm aperture, both of which are equipped for photo-polarimetry in the B, V, R, and I bands. For our observations, we have photometric data in these bands. BL Lac was observed as part of the TOP-MAPCAT blazar monitoring program (Agudo et al., 2012).

2.2.5 Millimetric Observations: IRAM

IRAM is a 30 m dish radio telescope operated by the *Instituto de Radioastronomía Milimétrica* and located at Sierra Nevada, in Granada, Spain. It observes in millimetric wavelengths, specifically in the 1.3 mm and 3 mm bands. IRAM observed BL Lac on two nights during the period studied here, in particular on the nights of October 28th and November 1st, 2022, as part of the POLAMI program, a Very Large Baseline Interferometry (VLBI) monitoring program for AGN running since 2006 (Agudo et al., 2018). Due to the very poor coverage provided by POLAMI, these data will only be used for the broadband SED interpretation presented in Section 3.3

2.2.6 Radio Observations: Metsähovi

Located in Finland, the *Metsähovi Radio Observatory* has been operational since 1974 and specializes in radio observations, particularly in the GHz range. In the context of the BL Lac observations, we obtained data of the radio LC at the frequency of 37 GHz.

3 | Analysis and Results

3.1 VHE emission

3.1.1 Detection of BL Lac in VHE gamma rays

Following the analysis procedure detailed in Section 2.1.3, we produced the overall θ^2 plot for BL Lac using all the available data, which cover 65 nights — 25 of them with LST-1 observations — and consist of a total observing time of 36 hours, making use of four wobble positions. This plot shows the cumulative significance for all observations, resulting in a detection with $\sigma = 27.75$ significance (see Fig. 3.1, which shows the θ^2 plot for all the data).
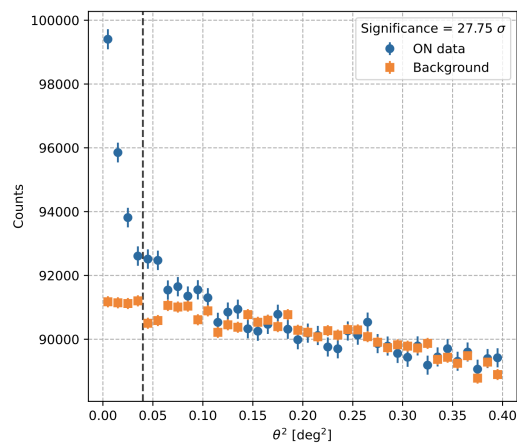

Figure 3.1: BL Lac θ^2 plot of detected activity between MJD 59843 (September 21st, 2022) and MJD 59908 (November 25th, 2022), for a total observation time of 37 h, with a significance of $\sigma = 27.75$. The ON and OFF distributions are shown in blue and orange, respectively.

Owing to the high significance detection after stacking all data, we have also produced
the θ^2 plots for each night with the goal of evaluating the detection on a daily basis
and have a first glimpse of the variability of BL Lac. Significance values of the θ^2
plots range from $\sigma = 0.01$ to $\sigma = 36.56$, with most nights having significance values
around 1 to 4 (refer to Table 3.1). The highest significance was detected during the
night MJD 59872 (October 20th, 2022) with $\sigma = 36.56$ (see Fig. 3.2, left panel). Another
night with an especially high significance was on MJD 59896 (November 13th, 2022),
with $\sigma = 27.14$ (see Fig. 3.2, right panel). The significance values for all nights are
reported in Table 3.1.

Table 3.1: Significance and flux level of BL Lac's emission for each observing night.
Upper limits to the flux are calculated as the 95% confidence level for flux points with
a significance <2σ.

Day	Observation Time (h)	Significance	Flux[a] ($\times 10^{-11}$ cm^{-2} s^{-1})	Day	Observation Time (h)	Significance	Flux[a] ($\times 10^{-11}$ cm^{-2} s^{-1})
21/09	1.65	0.74	3.19	26/10	1.23	3.88	12.88 ± 3.28
01/10	1.62	1.73	4.53	27/10	1.36	7.58	39.41 ± 3.72
03/10	2.86	2.44	3.36 ± 1.23	29/10	0.72	1.25	6.83 ± 2.04
15/10	1.31	9.05	27.23 ± 2.46	31/10	1.73	1.43	8.27 ± 1.28
16/10	0.04	0.81	34.33	01/11	1.27	3.27	6.1 ± 1.12
17/10	2.14	10.83	28.44 ± 2.24	13/11	1.51	27.14	65.68 ± 1.97
18/10	2.48	4.14	5.4 ± 2.11	14/11	0.32	0.35	7.73
19/10	2.67	4.85	17.61 ± 2.68	15/11	0.76	1.69	11.69
20/10	2.50	36.56	102.65 ± 2.6	16/11	0.85	2.14	20.64 ± 4.3
21/10	1.87	2.78	8.79	17/11	0.87	1.22	10.84 ± 3.86
23/10	1.41	1.98	16.64	18/11	1.01	2.16	10.64
24/10	0.27	0.67	17.06	19/11	0.57	0.46	7.63
25/10	2.19	0.01	7.26	25/11	0.70	7.88	50.71 ± 4.92

[a]Flux points without errors correspond to 2σ (95% confidence level) flux upper limits.

3.1.2 VHE gamma-ray LC and SED

To construct the spectrum and SED of BL Lac, we follow the procedure detailed in
Section 2.1.3. We began by characterizing the average state using all available data
and fitting it with a LogParabola spectral model. The resulting SED can be seen in
Fig. 3.3. We then performed a preliminary computation of the LC using the average
spectrum, which can be seen in Fig. 3.5. For the gamma-ray flux calculation and LC
production we use an energy threshold of 100 GeV.

However, due to the significant variability observed, we recognize that the average
spectrum might not be fully representative of the different flux states within the pe-
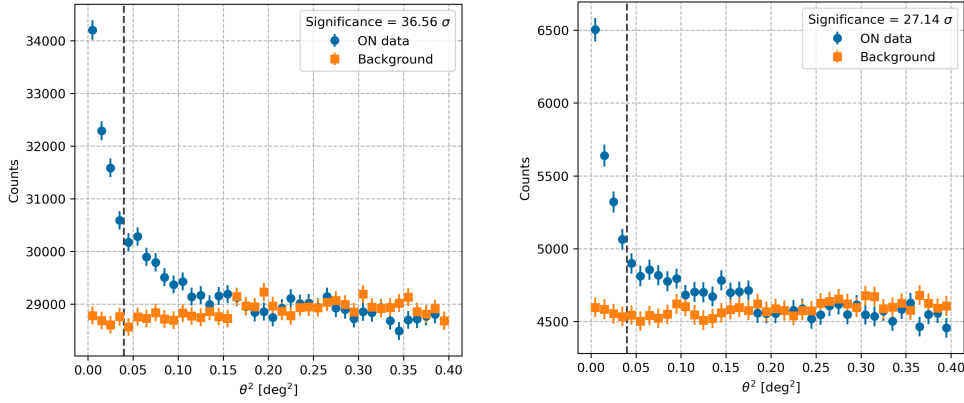
Figure 3.2: *Left:* BL Lac θ^2 plot of detected activity during MJD 59872 (October 20th, 2022), for a total observation time of 2.50 h, with a significance of $\sigma = 36.56$. *Right:* BL Lac θ^2 plot of detected activity during MJD 59896 (November 13th, 2022), for a total observation time of 1.51 h, with a significance of $\sigma = 27.14$. The ON and OFF distributions are shown in blue and orange, respectively.

riod. This spectral variability could lead to inaccuracies in the LC if the average spectrum were used throughout. To address this issue, we segment the preliminary LC calculated using the average spectrum into periods where the flux is relatively constant, and reconstruct the LC for each of these time intervals using the differential energy spectrum (DES) reconstructed for each of these periods. For this, we use an identification of periods with similar flux level based on a Bayesian Block (BB) representation (Scargle et al., 2013). This algorithm identifies an optimal way to segment the LC into states of roughly constant flux, where the average flux between two change points (cuts in the time axis) is considered the flux for the BB.

The different BBs of the preliminary LC of BL Lac were obtained using the `lightcurves` PYTHON package (Wagner et al., 2022), which implements the BB algorithm from Scargle et al. (2013). A false positive rate of 1% was used to find cuts that indicate when the source changes from one to another distinct state. We initially obtain 12 blocks (see Fig. 3.5), of which we recompute blocks 9, 10 and 11, merging them into a single one to accumulate enough number of events and statistics in order to produce a well-characterized spectrum of this period (hereafter block 9). Therefore, our BB representation divides the event period into ten BBs, with the two high flux peaks being represented by the fourth and eighth BBs (labelled BB4 and BB8, respectively).

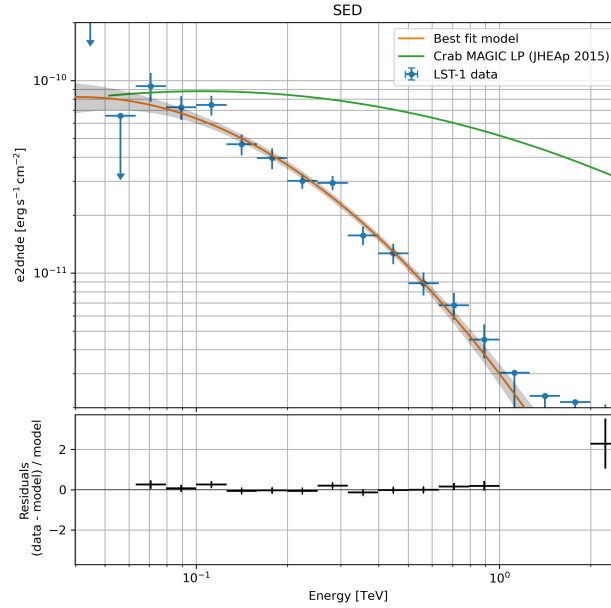The SEDs were then recreated for each of the ten BBs following the same process.

Figure 3.3: BL Lac average SED reconstructed using the LST-1 data, with the same selection masks as for the θ^2 plots. For reference, Crab SED as measured by MAGIC (Aleksić et al., 2015) is also shown in orange. Down-pointing arrows correspond to upper limits. Residuals are shown at the bottom panel. Fit parameters of the spectrum are reported in Table 3.2.

We characterized the spectrum for each BB (see Table 3.2), and generated their corresponding SEDs (see Fig. 3.4). Ultimately, making use of these SEDs, we recompute the overall LC block by block (see Fig. 3.6), resulting in a more accurate reconstruction of the VHE gamma-ray flux of BL Lac in periods of extreme variability. Two of the observed nights have measured fluxes that stand out as being significantly brighter than the reference Crab Nebula flux, corresponding to the two nights of greatest θ^2 significance (October 20th, 2022 and November 13th, 2022) corresponding to the θ^2 plots from Fig. 3.2, and to the aforementioned BBs 4 and 8, respectively. The average flux for all the data is $(1.65 \pm 0.49) \times 10^{-10}$ cm^{-2} s^{-1}, i.e. (0.35 ± 0.10) Crab Units (C.U.)[1], whereas it is $(1.02 \pm 0.03) \times 10^{-9}$ cm^{-2} s^{-1}, equivalent to (2.14 ± 0.06) C.U., for October 20th; and $(6.57 \pm 0.20) \times 10^{-10}$ cm^{-2} s^{-1}, that corresponds to (1.38 ± 0.04) C.U., for November 13th.

---

[1] 1 C.U. is the flux of the Crab Nebula above a certain energy; $(4.76 \pm 0.01) \times 10^{-10}$ cm^{-2} s^{-1} for $E > 100$ GeV.
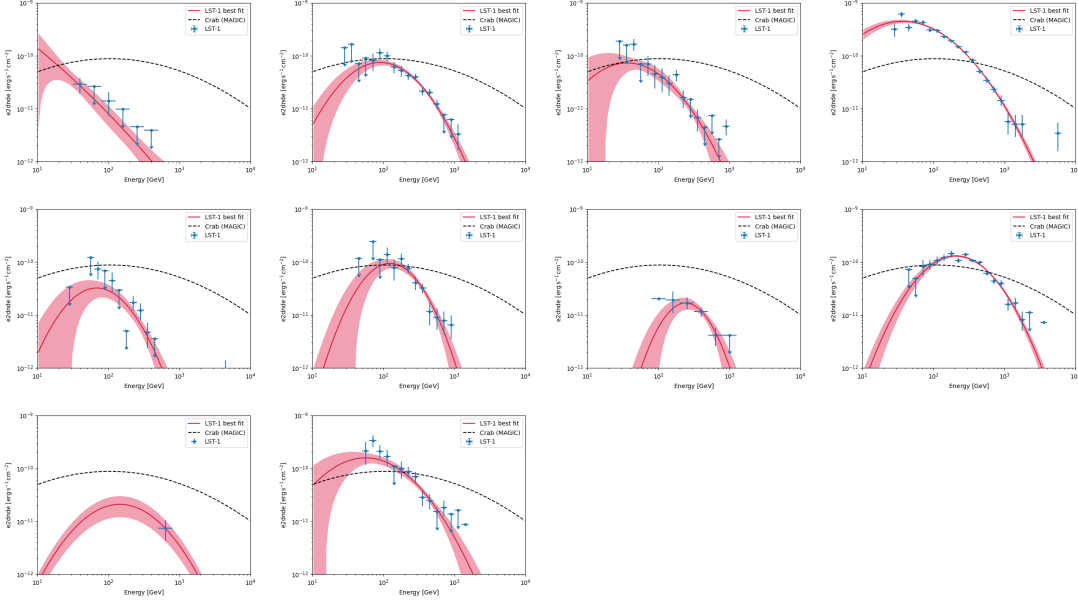
Figure 3.4: BL Lac SEDs computed for each BB. From left to right, then top to bottom, the plots correspond to the SEDs of BB1 through BB10.

Table 3.2: Spectral parameters for BL Lac's average emission state and for each BB, considering a LogParabola spectral model.

	Period	ϕ_0 $\left(\times 10^{-13}\,\mathrm{GeV}^{-1}\mathrm{s}^{-1}\mathrm{cm}^{-1}\right)$	E_0 (TeV)	α	β
Average	21/09 - 26/11	4.21 ± 0.17	0.22	3.09 ± 0.10	0.36 ± 0.07
BB1	21/09 - 10/10	35.08 ± 12.46	0.06	3.31 ± 0.35	0.06 ± 0.24
BB2	10/10 - 18/10	2.90 ± 0.23	0.28	3.28 ± 0.13	0.57 ± 0.13
BB3	18/10 - 20/10	16.55 ± 4.43	0.12	3.11 ± 0.18	0.47 ± 0.32
BB4	20/10 - 21/10	62.69 ± 2.04	0.15	2.95 ± 0.03	0.34 ± 0.03
BB5	21/10 - 27/10	5.91 ± 1.60	0.15	3.20 ± 0.35	0.78 ± 0.36
BB6	27/10 - 29/10	1.86 ± 0.22	0.34	3.98 ± 0.42	0.98 ± 0.36
BB7	29/10 - 08/11	0.04 ± 0.02	0.72	4.97 ± 1.27	1.36 ± 0.67
BB8	08/11 - 14/11	5.33 ± 0.22	0.36	2.68 ± 0.06	0.62 ± 0.07
BB9	14/11 - 23/11	0.08 ± 0.04	0.69	3.51 ± 0.01	0.48 ± 0.01
BB10	23/11 - 26/11	5.40 ± 0.75	0.26	3.28 ± 0.22	0.42 ± 0.18

3.1.3   Fast VHE gamma-ray variability

For the two brightest nights of October 20th and November 13th (corresponding to BB4 and BB8), LCs were computed to a minute-wise resolution using five-minute
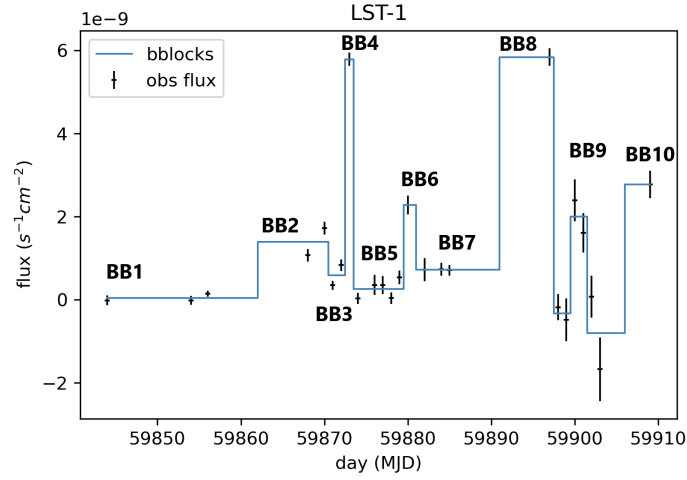
Figure 3.5: BL Lac preliminary LC above 100 GeV in black with the BB representation
in blue generated using a 1% false positive rate. The x-axis indicates time (in MJD) and
the y-axis indicates the flux (in $s^{-1}\ cm^{-2}$ units). For this analysis we have recomputed
the 9th, 10th and 11th BBs into a single one, resulting in a total of ten different BBs.

bins (see Fig. 3.7). We then evaluated the fastest variability timescales observed during
these two nights of particularly high significance using the exponential rise and decay
model from Abdo et al. (2010b). These rapid variations impose direct constraints on
the size of the emitting region through the causality relation defined by Eq. (1.1),
which will serve as a crucial parameter for the broadband fit of the multiwavelength
SED of the jet.

October 20th Flare: The brightest flare during the observation period was recorded
on October 20th, 2022, with the VHE gamma-ray flux increasing from less than 1 C.U.
to over 4 C.U. within approximately one hour (left panel of Fig. 3.7). To model this
variability, we used a two-component exponential function describing both the rise
and decay of the flare (Abdo et al., 2010b; MAGIC Collaboration et al., 2020),

$$F(t) = F_b + F_0 \left/ \left(e^{-(t-t_0)/t_{\text{rise}}} + e^{-(t-t_0)/t_{\text{decay}}} \right) \right. , \tag{3.1}$$

where F_b is a baseline flux, F_0 is the amplitude of the variability, $F(t)$ is the flux at time
t, and t_{rise} and t_{decay} represent the timescales of the flare's rise and decay, respectively.
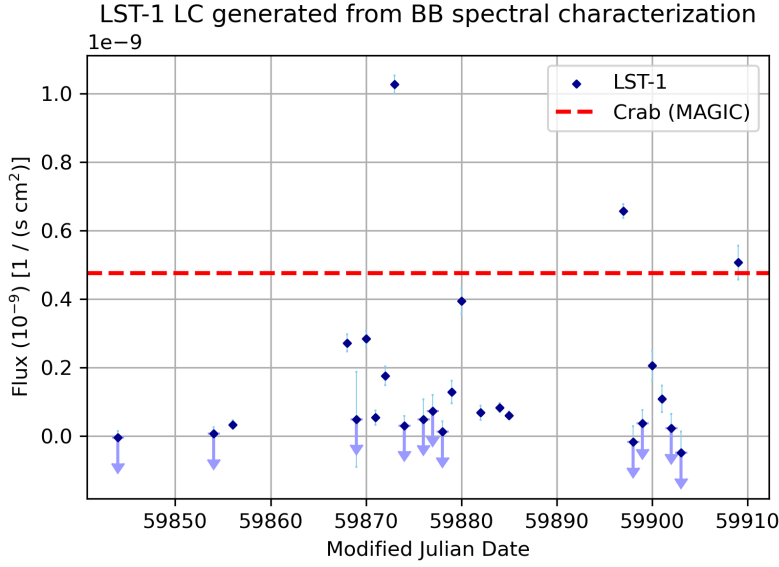This fitting was applied using 5-minute binned LCs to capture the fast variability.

Figure 3.6: BL Lac LC above 100 GeV reconstructed from the spectrum of each BB. Down-pointing arrows indicate upper limits. For reference, the Crab flux measured by MAGIC (Aleksić et al., 2015) is also shown.

We estimated the shortest timescale of variability using the flux-doubling criterion $t_{\text{var}} = t_{\text{rise/decay}} \times \ln 2$ (MAGIC Collaboration et al., 2020), where t_{var} represents the time over which the flux doubles. The shortest flux-doubling time was found to be $t_{\text{var}} = 20.83$ minutes. This rapid variability provides a direct constraint on the size of the emission region, which we estimate using the causality condition Eq. (1.1), and depending on the Doppler factor δ_D of the jet. With δ_D typically ranging from 10 to 50 (see for instance Liodakis et al., 2017), we find the size of the emission region for the October 20th flare to be $R \lesssim (3.51 - 17.53) \times 10^{14}$ cm.

November 13th Flare: For the night of November 13th, the LC produced from the BB8 spectrum shows a decaying profile (see Fig. 3.7, right panel), which we modeled using a decaying exponential function,

$$F(t) = F_b + F_0 e^{-(t-t_0)/t_{\text{decay}}}. \tag{3.2}$$

Similarly to the October 13th flare, we computed a shortest flux-doubling time of $t_{\text{var}} = 16.93$ minutes, and find the size of the emission region for the November 13th flare to be $R \lesssim (2.85 - 14.24) \times 10^{14}$ cm.
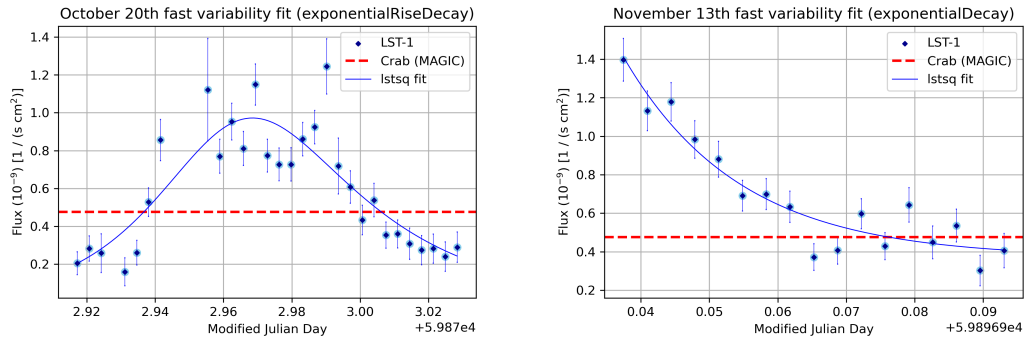
Figure 3.7: *Left:* Minute-wise LC above 100 GeV for BB4 (October 20th). A fit (R = 0.74) to Eq. (3.1) is shown in blue, with parameters $t_0 = 59872.96$, $F_0 = 0.95$ cm^{-2} s^{-1}, $t_{rise} = 0.021 \pm 0.009$ d, $t_{decay} = 0.032 \pm 0.016$ d, $F_b = 0.20$ cm^{-2} s^{-1}. *Right:* Minute-wise LC above 100 GeV for BB8 (November 13th). A fit (R = 0.90) to Eq. (3.2) is shown in red, with parameters $t_0 = 59896.93$, $F_0 = 1.09$ cm^{-2} s^{-1}, $t_{rise} = 0.017 \pm 0.004$ d, $F_b = 0.37$ cm^{-2} s^{-1}. For reference, the Crab flux measured by MAGIC is also shown.

3.2 Multiwavelength emission

We merged multiwavelength observations into their respective bands for the BL Lac flare event (see Fig. 3.8) to study the variability and correlations of the LCs. From an initial qualitative observation of the data, we find the *Fermi*-LAT LC has a single flare day of significant activity above base flare activity, on October 16th; in the XRT LC we find a flare of significant activity above its base flare activity on November 12th, possible precursor of the VHE gamma-ray flare from November 13th, day during which XRT did not observe. We also find the LCs of UVOT to be highly cross-correlated across its filters, and the optical *BV RI* bands show cross-similarity in its activity.

We have evaluated the potential presence of correlated emission among the different bands of the spectrum. For this we have use the `mutis`[2] PYTHON package, to compute the correlation of a pair of signals and estimate its significance by generating synthetic LCs through a MC process implementing the (Welsh, 1999) algorithm for discrete signals non-uniformly sampled in time. We generated the 1000 synthetic LCs for each of every pair of signals, using randomization of the Fourier transform from the power spectral distribution. The synthetic LCs are generated with the same statistical properties (power spectral density, probability density function, time coverage

---

[2]MUltiwavelength TIme Series (https://github.com/IAA-CSIC/MUTIS). A Python package for the analysis of correlations of LCs and their statistical significance.
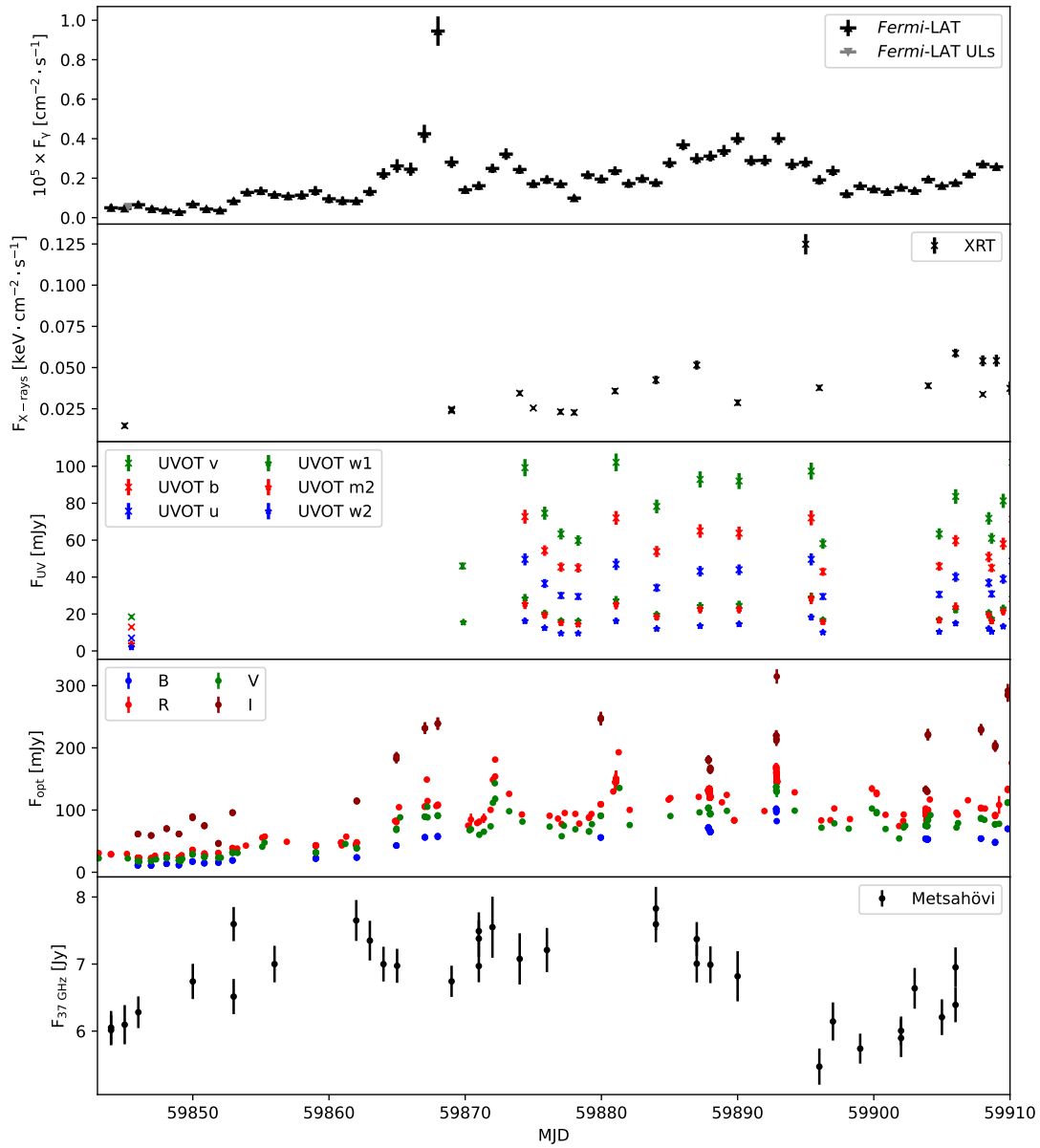
Figure 3.8: Multiwavelength LCs of BL Lac between September and November 2022. From top to bottom: HE gamma rays (*Fermi*-LAT), X-rays (*Swift*-XRT), UV-optical (*Swift*-UVOT), optical *BV RI* (ZTF, IAC80, SNO, LCOGT, Tuorla Observatory), radio 37 GHz (Metsahövi).

and sampling) as the real signals for the significances to be representative. We used uniform time binning of size 10 days, large enough to reach enough statistics and small enough that correlations were not smoothed too much.

The correlation plots show the interband correlations and significances computed with a running window for time differences between the signals (x-axis). Among the data we have, the R band has the largest amount of data points and was hence used as reference for the correlation analysis (see Fig. 3.9 for the different correlations with respect to the R band). Estimating to nearest multiples of 5 days, we find significant (3σ) synchronous ($-5 \lesssim \tau \lesssim +10$ days) correlation with the HE gamma-ray emission, with maximum correlation around zero delay, showing strong synchronicity and suggesting contemporaneous emission at both optical and gamma-ray wavelengths; and $-30 \lesssim \tau \lesssim +0$ days with XRT, with maximum correlation around -15 days, maybe suggesting a delayed response of the X-ray emission to the optical variability, however still compatible with no delay. We also observe $-50 \lesssim \tau \lesssim -15$ days significant delays with the bb-band UVOT data, with maximum correlation around -40 days; $-5 \lesssim \tau \lesssim +20$ days delays with the optical V band, showing strong synchronicity with the correlation peaking around +5 days; and $-10 \lesssim \tau \lesssim +0$ days delays with radio data, with the correlation peaking at -5 days.

The results obtained on the different LCs indicate that the multiwavelength emission shows a non-delayed, highly correlated behaviour along the different bands. We note that the correlations with the X-ray and optical-UV UVOT bands are affected by the much lower amount of *Swift* data, that is especially noticeable during the first half of the period. Therefore, even if the maximum correlation happens at a delay slightly shifted from zero, this smaller sampling introduces larger errors in the determination of the correlations, making most likely these signals still compatible with zero delay. Additionally, we are not able to evaluate the correlation with the VHE gamma-ray LC. This is because this band consists only of a few flux points due to the limited monitoring capability of LST-1 and the presence of flux upper limits for those nights with low gamma-ray activity.

3.3 BL Lac Broadband SED

Finally, compiling all the multiwavelength and VHE gamma-ray data, we have constructed the average broadband SED of BL Lac during the studied period, with the aim of modeling the emission across the electromagnetic spectrum with a leptonic
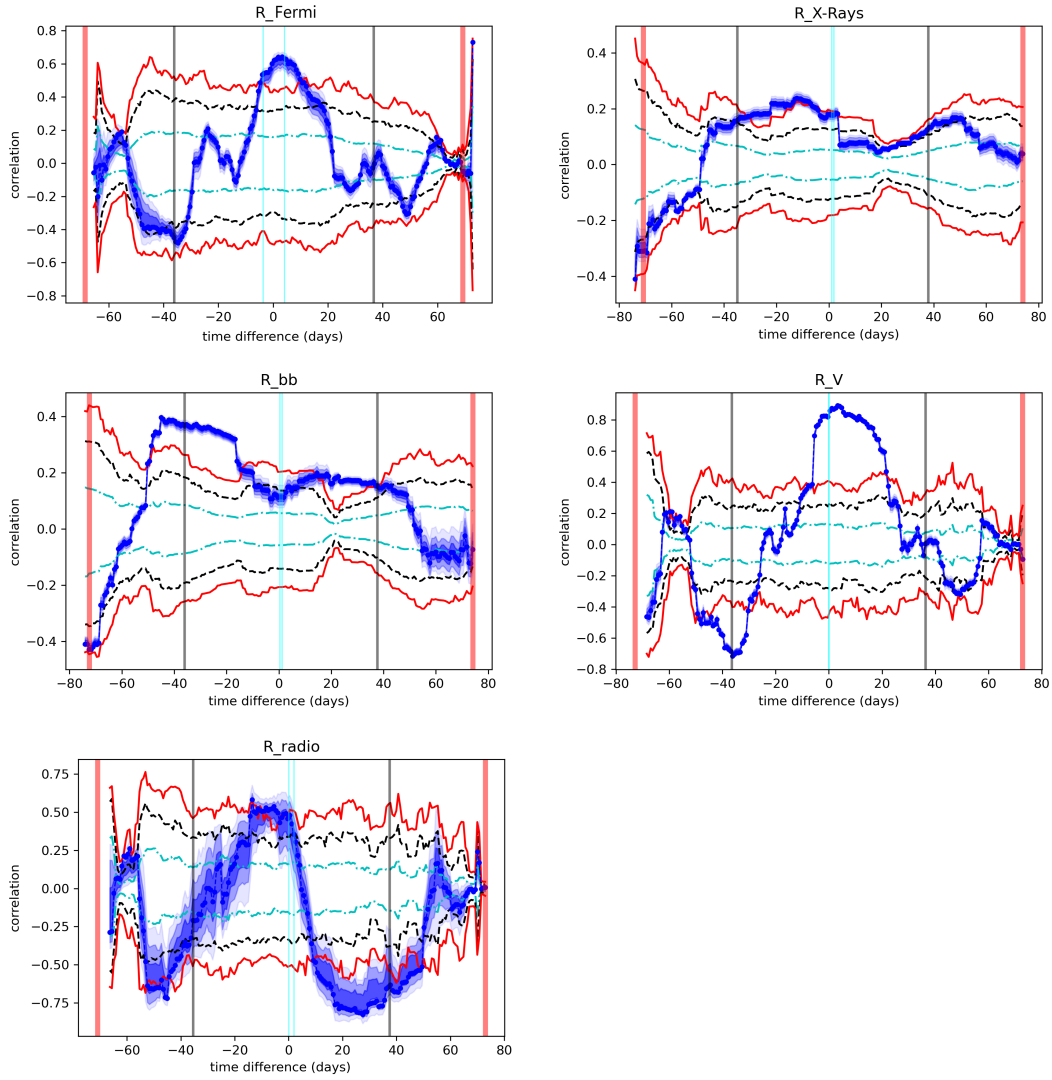
Figure 3.9: Interband correlation curves during the BL Lac observation period. From left to right, then top to bottom: correlations of the R band LC with the HE gamma-ray, X-ray, UV-optical (bb filter), optical (V filter), and radio LCs. The dashed aqua, black and red lines show significance levels of 1σ, 2σ and 3σ, respectively.

emission model, characterizing the emission by a low-energy peak from synchrotron emission and a high-energy peak from a leptonic SSC process. The simplest approach to model the broadband SED is a one-zone SSC emission model, assumed to originate from a single homogeneous region in the jet (Tavecchio et al., 1998). However, for extreme flares like the ones observed in BL Lac during this period, the one-zone model is often inadequate. Previous studies (see for instance MAGIC Collaboration et al., 2019b) have demonstrated that such a model fails to accurately reproduce the high flux levels and spectral variability observed during intense flare events.

Therefore, we adopt a more complex two-zone SSC model, which allows for a better representation of the data during this high-activity period. Another alternative would be considering an external radiation field (accretion disk, dusty torus and BLR) that provides low energy photons that produce the observed gamma-ray emission via IC. However, BL Lacs are known for having very weak or even absence of these components (see MAGIC Collaboration et al., 2019b), hence not being physically realistic.

We assume the two-zone model of Tavecchio et al. (2011), where the emission originates from two spherical co-spatial, physically separated regions, called "core" and "blob", with sizes $R_{\text{core}} > R_{\text{blob}}$. Similarly to the one-zone SSC model, each of the two regions is characterized by a set of physical parameters including the magnetic field strength B, the Doppler factor δ_D, the Lorentz factor Γ, and size of the emitting region R, that are able to model the synchrotron and SSC radiation emitted by them. Each region has its own population of relativistic particles – electrons in leptonic models – that are assumed to follow a broken power law distribution with the Lorentz factor,

$$N(\gamma) = K\gamma^{-n_1}\left(1 + \frac{\gamma}{\gamma_b}\right)^{n_1 - n_2}, \quad \gamma_{\text{min}} < \gamma < \gamma_{\text{max}}, \tag{3.3}$$

being γ_{min} and γ_{max} the minimum and maximum Lorentz factors of the electrons, n_1 and n_2 the spectral indices of the particle distribution below and above the break Lorentz factor γ_b, and K the normalization constant of the distribution.

To model the broadband SED of the entire observation period we use the `agnpy` PYTHON package, which provides tools to model the emission from AGN jets with various radiative processes among which we find the leptonic scenarios considered here (Nigro et al., 2022; Nigro et al., 2023). We model the average emission state of BL Lac over the observation period to provide a representative view of the source's behaviour. The blob is a more compact and energetic region than the core. Therefore, its gamma-ray IC emission will reach higher energies than that from the core, being re-
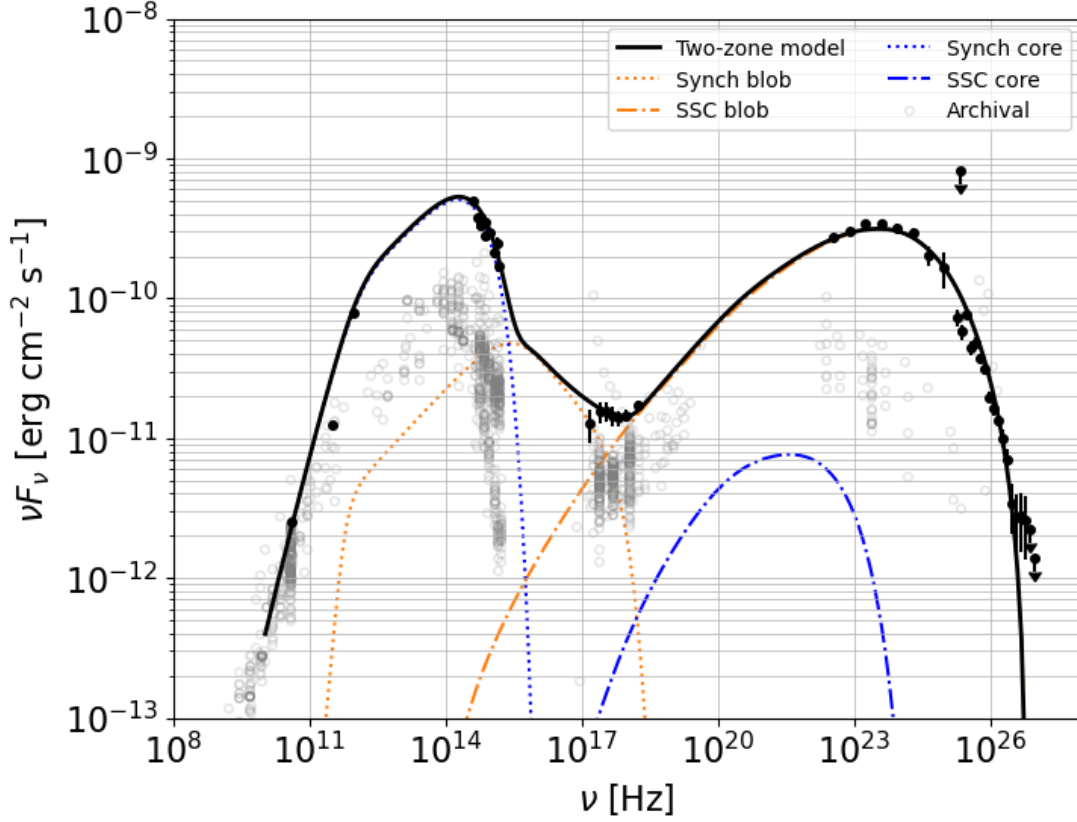
Figure 3.10: Broadband SED of BL Lac using a two-zone SSC leptonic model. The black solid line corresponds to the fitted model. Dotted/dash-dotted blue and orange lines correspond to the synchrotron/SSC emission of blob and core, respectively. Shadow markers correspond to archival data retrieved from the Space Science Data Center (SSDC) database (`https://tools.ssdc.asi.it/SED/`, see Stratta et al., 2011).

sponsible for the observed gamma-ray radiation and variability observed by the LAT and LST-1. On the other hand, the core is expected to be less dense and energetic, hence contributing more at lower energies, i.e. radio and optical. In consistency with the fast gamma-ray variability analysis (Section 3.1.3), we limit the size of the blob to a value $R = 10^{15}$ cm. Finally, as introduced in Section 1.3.2, the EBL absorbs a fraction of the gamma rays emitted by extragalactic sources on their way to Earth. Therefore, in order to account for EBL gamma-ray absorption and model the intrinsic emission of BL Lac, we correct the SED according to the model from Saldana-Lopez et al. (2021). The broadband SED and two-zone SSC model fitting are shown in Fig. 3.10, with the parameters describing the model listed in Table 3.3.

Table 3.3: Parameters used for the blob and core components of the two-zone leptonic SED emission model of BL Lac shown in Fig. 3.10.

Region	γ_{min} $(\times 10^3)$	γ_b $(\times 10^4)$	γ_{max} $(\times 10^5)$	n_1	n_2	B (G)	K (cm^{-3})	R $(\times 10^{15}\,cm)$	δ_D	Γ
Blob	0.01	1.15	1.5	2.3	3.75	0.15	0.4e-2	1	40	40
Core	0.4	0.6	0.12	2.3	2.9	0.1	0.12e-6	650	15	15

We observe that we can successfully reproduce the observed broadband emission from BL Lac with a two-zone leptonic SSC model. We note that the second and third spectral points[3] coming from LST-1 slightly deviate from the fitted model — however they are still consistent within approximately a 2σ confidence level. This deviation is likely influenced by systematic errors, more important at energies of a few GeV (Abe et al., 2023b), and since moonlight data were not considered, also impacting more LST-1's lowest energies, we consider this deviation acceptable. Additionally, the two radio points at higher frequencies, originating from POLAMI only have two observations during this period. As a result, they are not as representative of the average emission state but reflect only two specific days. Therefore, we prioritize modeling the Metsähovi 37-GHz data, which is at a lower frequency and is well-aligned with the average state.

We compare our results with the typical value ranges used to model the SED of a large blazar sample presented by (Ghisellini et al., 2010), and all the values we use are consistent; with the necessity of a large Lorentz and Doppler factor than usual for blazars, in order to explain the very strong flare in gamma rays. However, we note that this has been observed before in these extreme cases (Aharonian et al., 2007; Albert et al., 2007; MAGIC Collaboration et al., 2018). It is important to note SED models like the two-zone model used in this work are limited by parameter degeneracy — meaning that other combinations of parameters might also result in optimal fits from a statistical point of view. Within this context, the fit parameters of the observed SED where chosen to result in a physically sound representation of the broadband emission.

---

[3]The first LST-1 SED data point corresponds to a frequency of 1.7×10^{25} Hz, right before the *Fermi*-LAT flux upper limit. All points at frequencies above LAT's upper limit are from LST-1.

4 | Discussion

The VHE gamma-ray flare of BL Lac observed in this campaign ranks among the brightest ever recorded, only comparable to the historical flare from 2021 as detailed by Nozaki et al. (2023). The extreme flux increase and rapid variability underscore the compactness of the emission region, as previously proposed in the context of the causality relation (Aharonian et al., 2007). The size of the emitting region, constrained by the flux doubling times observed, suggests that the gamma-ray emission originates from a very small, compact region ($R \lesssim 10^{15}$ cm).

The timescales of the rapid variability observed in VHE gamma-rays point towards either shock acceleration or magnetic reconnection (Jormanainen et al., 2023). However, based on recent studies, magnetic reconnection is increasingly favored as the dominant mechanism, as it requires relatively moderate Lorentz factors compared to shock acceleration, which requires very high Lorentz factors (Henri & Saugé, 2006). Recent evidence from blazar studies, such as that by Jormanainen et al. (2023), support the notion that magnetic reconnection drives such rapid particle acceleration, particularly in blazars like BL Lac, where we observe ultra-fast flaring.

The correlations found across the multiwavelength LCs, especially between HE gamma-rays and optical, suggest that the emissions are largely co-spatial, meaning they originate from the same regions. Such correlations have been widely reported in other blazar studies (see for instance Blasi et al., 2013; Priya et al., 2022), and in the case of BL Lac, they reinforce the idea that the different emission processes — synchrotron radiation at low energies and IC scattering at higher energies — are driven by the same populations of particles within localized regions.

The observed SED is consistent with emission of leptonic origin. This conclusion aligns with the fact that BL Lac is not expected to be a strong neutrino source as per IceCube observations (Paiano et al., 2021). This implies that hadronic processes are not dominant in BL Lac, reinforcing the interpretation of the gamma-ray emission
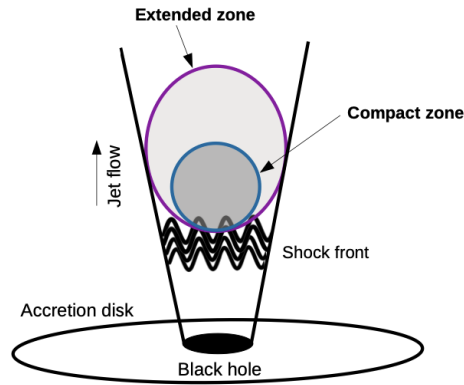
Figure 4.1: Sketch of the pseudo-stratified jet model assumed in this work in the recent work on the blazar Mrk 501 by MAGIC Collaboration et al. (2024). Credit: MAGIC Collaboration et al. (2024).

being primarily leptonic, in consistency with our modeling.

This is also supported by the results derived thanks to the recent launch of the Imaging X-ray Polarimetry Explorer (IXPE, see Weisskopf et al., 2016) through the study of the X-ray and broadband polarized emission of blazars. In the case of BL Lac, where during the low emission states the X-ray emission is predominantly produced by IC scattering, i.e. it behaves as a LBL blazar, the expected X-ray polarization degree is much lower than that at optical wavelengths (Peirson & Romani, 2019; Liodakis et al., 2019), as found by Middei et al. (2023). On the other hand, during flaring states it becomes an IBL, shifting its synchrotron peak frequency towards higher energies. In this scenario, the X-ray emission is mainly produced via synchrotron radiation and hence, it is expected to be as or more polarized than that in the optical regime (Peirson & Romani, 2019; Liodakis et al., 2019). This was favoured by Peirson et al. (2023) with almost simultaneous observations by IXPE to those presented in this work by LST-1 (only 3 days after the last LST-1 observation used in this work).

Finally, the results obtained by IXPE since its launch for already several blazars support the hypothesis of an energy-stratified structure of the relativistic jet (see Fig. 4.1 and Liodakis et al., 2022). This comes from the comparison of the radio, optical and X-ray polarization degree behaviour, in comparison with that expected from theoretical models and simulations (Peirson & Romani, 2019; Liodakis et al., 2019). Even if the model performed here is an oversimplification of this scenario, it is as a first order approximation consistent with the expected morphology of the jet. This was also observed for instance for the blazar Mrk 501 (MAGIC Collaboration et al., 2024).

5 | Conclusions and Future Work

5.1 Conclusions

We have characterized the VHE gamma-ray emission of blazar BL Lacertae during a flaring period observed by LST-1 between September and November 2022, ranking among the brightest ever recorded, with average emission of 0.35 ± 0.10 C.U. and a highest flux of about 3 C.U., comparable to the historical flare from 2021. We have also characterized the VHE gamma-ray spectrum, which shows a LogParabolic shape with clear curvature. Through a BB analysis we have identified periods of relatively constant flux, showing intense spectral and flux variability from one to another.

We have observed fast intranight variability in two very bright nights. By modeling the corresponding LCs with exponential fits we were able to constrain the smallest observed variability timescales of ∼17 min, providing limits to the size of the gamma-ray emitting region, computed to be of the order 10^{15} cm. Therefore, we conclude that this fast variability must come from an inner, compact region of the relativistic jet.

The multiwavelength LCs also show very prominent flares, with *Fermi*-LAT and XRT showing the highest variability. Moreover, the interband correlation analysis performed on the multiwavelength LCs is in agreement with correlated emission consistent with zero time lag, supporting the idea that these emissions are co-spatial.

Finally, we have modeled the broadband emission with a two-zone leptonic SED model. This model assumes a co-spacial and pseudo-stratified jet, with an internal and compact "blob" region, responsible for the observed VHE gamma-ray variability; and a larger and less energetic "core" component, responsible for the radio-to-optical and X-ray emission. The leptonic nature of the emission and the assumed structure of the jet for the model presented here are in agreement with the results obtained by IXPE through X-ray and broadband polarization observations.

5.2 Future Work

The LST-1 data used in this work includes some nights of observations under moonlight conditions, that were however treated as first approximation as dark data. To improve the precision of the VHE gamma-ray flux measurements, particularly at energies of a few GeV, the LST-1 analysis of this subset of data can be refined by implementing specific data treatment, applying a more aggressive cleaning to minimize the background signal introduced by the Moon.

Moreover, a detailed spectral variability analysis of the X-ray, HE and VHE gamma-ray spectrum would help constrain the distribution of the electron population responsible for the emission through the understanding of how the spectral shape changes over time. This could lead to a more accurate modeling of the broadband emission, using a more realistic particle population distribution.

Radio VLBI observations, with their resolution under the order of milliarcseconds, would allow us to resolve different components of the jet, which could be used to track their propagation along the jet and provide measurements of the structural evolution over time. The detection of superluminal motion of the identified components could also be used to set observational constrains to parameters that play an important role in the description of the broadband emission such as the Lorentz factor Γ.

Although the two-zone pseudo-stratified jet model fits the observational data, it is most likely a simplification to the complexity of the real structure of a relativistic jet. This could be improved in the future, as models keep being upgraded and refined. Moreover, the modeling was performed on the average emission state. A more sophisticated approach would involve using using temporal series of SEDs and a time-dependent SED model, accounting for the variability observed in the SEDs and their relationship to the components of the jet. In this way, we might be able to explain the observed variability from the point of view of the physical parameters describing the intrinsic emission of the source.

Bibliography

Abdo A. A., et al., 2010a, Science, 329, 817

Abdo A. A., et al., 2010b, ApJ, 722, 520

Abe H., et al., 2023a, ApJ, 956, 80

Abe H., et al., 2023b, ApJ, 956, 80

Acciari V. A., et al., 2020, ApJS, 247, 16

Adams C. B., et al., 2021, ApJ, 923, 241

Adams C. B., et al., 2022, ApJ, 932, 129

Agarwal S., et al., 2023, MNRAS, 521, L53

Agudo I., et al., 2012, International Journal of Modern Physics: Conference Series, 08, 299–302

Agudo I., et al., 2018, MNRAS, 474, 1427

Aharonian F., et al., 2007, ApJL, 664, L71

Albert J., et al., 2006, ApJL, 638, L101

Albert J., et al., 2007, ApJ, 669, 862

Aleksić J., et al., 2012, A&A, 544, A142

Aleksić J., et al., 2015, Journal of High Energy Astrophysics, 5, 30

Atwood W. B., et al., 2009, ApJ, 697, 1071

Ballet J., et al., 2023, arXiv e-prints, p. arXiv:2307.12546

Beckmann V., Shrader C., 2012, Active Galactic Nuclei. Wiley, doi:10.1002/9783527666829

Bednarek W., Bartosik M., 2003, A&A, 405, 689

Bellm E. C., et al., 2019, PASP, 131, 018002

Blandford R. D., Königl A., 1979, ApJ, 232, 34

Blandford R., Meier D., Readhead A., 2019, ARA&A, 57, 467

Blasi M. G., et al., 2013, A&A, 559, A75

Bradt H. V., Rothschild R. E., Swank J. H., 1993, A&AS, 97, 355

Brown T. M., et al., 2013, PASP, 125, 1031

Browning R., Ramsden D., Wright P. J., 1971, Nature Physical Science, 232, 99

Burrows D. N., et al., 2004, in X-Ray and Gamma-Ray Instrumentation for Astronomy XIII. pp 201–216, doi:10.1117/12.504868

CTA Consortium 2019, Astroparticle Physics, 111, 35

CTA-LST Project 2019, in 36th International Cosmic Ray Conference (ICRC2019). p. 653 (arXiv:1907.10146), doi:10.22323/1.358.0653

Cherenkov P. A., 1934, Comptes Rendus (Doklady) de l'Aeademie des Sciences de l'URSS, 2, 451

Costamante L., et al., 2001, A&A, 371, 512

Dermer C. D., Schlickeiser R., 1993, ApJ, 416, 458

Donath A., et al., 2023, A&A, 678, A157

Ertley C., 2014, in American Astronomical Society Meeting Abstracts #223. p. 118.03

Fomin V. P., et al., 1994, Astroparticle Physics, 2, 137

Funk S., 2008, Advances in Space Research, 41, 464

Gehrels N., Chipman E., Kniffen D., 1994, ApJS, 92, 351

Gerward L., 1999, Physics in Perspective, 1, 367–383

Ghisellini G., et al., 2010, MNRAS, 402, 497

Gould R. J., Schréder G., 1966, Physical Review Letters, 16, 252

Hartman R. C., et al., 1992, ApJL, 385, L1

Henri G., Saugé L., 2006, ApJ, 640, 185

Hess V. F., 1912, Phys. Zeit, 13, 1084

Hillas A. M., 1985, in 19th International Cosmic Ray Conference (ICRC19). p. 445

Hovatta T., Lindfors E., 2019, NewAR, 87, 101541

Jormanainen J., et al., 2023, A&A, 678, A140

Khachikian E. Y., Weedman D. W., 1974, ApJ, 192, 581

Klebesadel R. W., Strong I. B., Olson R. A., 1973, ApJL, 182, L85

Konigl A., 1981, ApJ, 243, 700

Li T. P., Ma Y. Q., 1983, ApJ, 272, 317

Liodakis I., et al., 2017, MNRAS, 466, 4625

Liodakis I., Peirson A. L., Romani R. W., 2019, ApJ, 880, 29

Liodakis I., et al., 2022, Nature, 611, 677

López-Coto R., et al., 2022, in Astronomical Data Analysis Software and Systems XXX.
    p. 357

López-Oramas A., 2015, PhD thesis, doi:10.13140/RG.2.1.4140.4969

MAGIC Collaboration et al., 2018, A&A, 617, A30

MAGIC Collaboration et al., 2019a, Nature, 575, 455

MAGIC Collaboration et al., 2019b, A&A, 623, A175

MAGIC Collaboration et al., 2020, A&A, 638, A14

MAGIC Collaboration et al., 2024, A&A, 685, A117

Maraschi L., Ghisellini G., Celotti A., 1992, ApJL, 397, L5

Massaro E., et al., 2009, A&A, 495, 691

Middei R., et al., 2023, ApJL, 942, L10

Miller J. S., French H. B., Hawley S. A., 1978, ApJL, 219, L85

Millikan R. A., 1926, Scientific American, 134, 149

Netzer H., 2013, The Physics and Evolution of Active Galactic Nuclei. Cambridge University Press

Netzer H., 2015, ARA&A, 53, 365

Nigro C., et al., 2022, A&A, 660, A18

Nigro C., et al., 2023, agnpy, doi:10.5281/zenodo.7633553

Nilsson K., et al., 2007, A&A, 475, 199

Nilsson K., et al., 2018, A&A, 620, A185

Nozaki S., et al., 2023, arXiv e-prints, p. arXiv:2309.09715

Padovani P., Giommi P., 1995, ApJ, 444, 567

Paiano S., et al., 2021, MNRAS, 504, 3338

Paxton L. J., Anderson H. R., 1992, The Journal of the Astronautical Sciences, 40, 305

Peirson A. L., Romani R. W., 2019, ApJ, 885, 76

Peirson A. L., et al., 2023, ApJL, 948, L25

Peterson B. M., 1997, An Introduction to Active Galactic Nuclei. Cambridge University Press

Peterson B. M., 2006, in Alloin D., ed., , Vol. 693, Physics of Active Galactic Nuclei at all Scales. p. 77, doi:10.1007/3-540-34621-X_3

Poole T. S., et al., 2008, MNRAS, 383, 627

Priya S., et al., 2022, MNRAS, 513, 2239

Rao M. V. S., Sreekantan B. V., 1998, Extensive Air Showers. World Scientific, doi:10.1142/3307

Ribó M., 2008, Chinese Journal of Astronomy and Astrophysics Supplement, 8, 98

Richmond M., 2024, Radio Astronomy: An Introduction, `http://spiff.rit.edu/classes/ast613/lectures/radio_i/radio_i.html`

Roming P. W. A., et al., 2005, Space Science Reviews, 120, 95

Rybicki G. B., Lightman A. P., 1979, Radiative Processes in Astrophysics. Wiley-VCH

Saldana-Lopez A., et al., 2021, MNRAS, 507, 5144

Scargle J. D., et al., 2013, arXiv e-prints, p. arXiv:1304.2818

Schlafly E. F., Finkbeiner D. P., 2011, ApJ, 737, 103

Schmidt M., 1963, Nature, 197, 1040

Seyfert C. K., 1943, ApJ, 97, 28

Shakura N. I., Sunyaev R. A., 1973, A&A, 500, 33

Stratta G., et al., 2011, arXiv e-prints, p. arXiv:1103.0749

Takalo L. O., et al., 2008, in American Institute of Physics Conference Series. AIP, pp 705–707, doi:10.1063/1.3076774

Tavecchio F., Maraschi L., Ghisellini G., 1998, ApJ, 509, 608

Tavecchio F., et al., 2011, A&A, 534, A86

Urry C. M., Padovani P., 1995, PASP, 107, 803

VERITAS Collaboration et al., 2009, Nature, 462, 770

Vassiliev V. V., 2000, Astroparticle Physics, 12, 217

Véron-Cetty M. P., Véron P., 2000, The Astronomy and Astrophysics Review, 10, 81

Wagner S. J., Witzel A., 1995, ARA&A, 33, 163

Wagner S. M., et al., 2022, in 37th International Cosmic Ray Conference. p. 868, doi:10.22323/1.395.0868

Weisskopf M. C., et al., 2016, Results in Physics, 6, 1179

Welsh W. F., 1999, PASP, 111, 1347

Wilson A. S., Colbert E. J. M., 1995, ApJ, 438, 62